scientific reports

Check for updates

OPEN

Optimization of automatic generation controllers in renewable multi-area power systems using the Fata Morgana algorithm

Aykut Fatih Güven[1]✉, Erdinç Şahin[2,3], Onur Özdal Mengi[4], Mohit Bajaj[5,6,7]✉ & Viktoriia Bereznychenko[8]✉

The increasing integration of renewable energy sources introduces severe intermittency in multi-area power systems (MAPS), resulting in significant voltage and frequency fluctuations. This study addresses this problem by implementing an automatic generation control (AGC) framework for a two-area hybrid power system composed of solar, wind, and thermal units. Four types of controllers (PI, PIDn, fractional-order PI (FOPI), and predictive PIDn (PPIDn)) were optimized using four recent metaheuristic algorithms: golden jackal optimization (GJO), educational competition optimizer (ECO), escape algorithm (ESC), and the newly proposed Fata Morgana Algorithm (FATA). The results demonstrate that the FATA-optimized PIDn controller provides the best dynamic performance, achieving an ITAE value of 0.18676, which represents an improvement of over 4.6% compared to the best established optimizer (ESC). Real-time validation on the OPAL-RT OP5707 platform confirmed the practical feasibility of the proposed FATA-based control strategy, verifying its ability to enhance frequency stability. These findings highlight the novelty and efficiency of FATA in optimizing AGC parameters for renewable-based multi-area power systems.

Keywords FATA, Multi area power systems, Meta-heuristic algorithms, Optimization, Real-time simulation

Abbreviations

2DOF	PDNTwo degrees of freedom proportional derivative with filter
2DOFPID	Two degrees of freedom FPID controller
3DOF-PDN	Three degrees of freedom proportional derivative with filter
ACE	Area control error
ACO	Ant colony optimization
AHB	Artificial humming bird
ALO	Ant-lion optimization algorithm
ANFIS	Artificial neuro fuzzy inference systems
ANN	Artificial neural networks
BB-BC	Big bang-big crunch
BOA	Bear optimization algorithm
CBO	Chaotic butterfly optimization
COA	Cuckoo optimization algorithm
GOA	Grasshopper optimization algorithm
CSOA	Crow search optimization algorithm
DOF-PDN	Degree of freedom proportional derivative with filter

[1]Department of Electrical and Electronics Engineering, Yalova University, Yalova, Turkey. [2]Department of Computer Engineering, Giresun University, Giresun, Turkey. [3]Department of Electrical and Computer Engineering, University of New Brunswick, Fredericton, Canada. [4]Department of Electrical and Electronics Engineering, Giresun University, Giresun, Turkey. [5]Department of Electrical Engineering, Graphic Era (Deemed to be University), Dehradun 248002, India. [6]Hourani Center for Applied Scientific Research, Al-Ahliyya Amman University, Amman, Jordan. [7]Graphic Era Hill University, Dehradun 248002, India. [8]Department of Theoretical Electrical Engineering and Diagnostics of Electrical Equipment, Institute of Electrodynamics, National Academy of Sciences of Ukraine, Beresteyskiy 56, 03680, Kyiv, Ukraine. ✉email: afatih.guven@yalova.edu.tr; mohitbajaj@ammanu.edu.jo; vika.bereznichenko@i.ua

DRLB	Deep reinforcement learning based
DWCA	Discrete water cycle algorithm
ECO	Educational competition optimizer
ESC	Escape optimization algorithm
FATA	Fata morgana algorithm
FHODFC	Fractional high order differential feedback controller
FLPID	Fuzzy logic integrated PID
FLC	Fuzzy logic controller
FOPI	Fractional order proportional-integral
FOPID	Fractional order proportional-integral-derivative
FOPID-PR	Fractional order proportional integral derivative-proportional resonant
FOTID	Fractional order-based tilt-Integral-derivative
FSO	Firebug swarm optimization
GA	Genetic algorithm
GJO	Golden jackal optimization
GWO	Grey wolf optimization
hGWO-PS	Hybrid grey wolf optimization-pattern search
HODFC	High order differential feedback controller
HSCOA	COA into harmony search (hs) algorithm
IAE	Integral of absolute error
ISE	Integral square error
ITAE	Integral of time weighted absolute error
ITSE	Integral of time square error
LMA	Levenberg marquardt algorithm
MAPS	Multi area power system
MFO	Moth flame optimizer
mMSA	Modified moth swarm algorithm
PDN	Proportional-derivative with filter
PI	Proportional-integral
PID	Proportional-integral-derivative
PIDn	Proportional-integral-derivative with filter
PPIDn	Predictive PID with filter
PPIDn	Predictive proportional-integral-derivative with filter
PSO	Particle swarm optimization
PV	Photovoltaic panel
SAR	Search and rescue
SCA	Sine–cosine algorithm
SOA	Skill optimization algorithm
SSA	Salp swarm algorithm
TAPS	Two area power system
TIDDF	Tilt-integral-double derivative filter
TLBO	Teaching learning-based optimization
WCA	Water cycle algorithm
P_line12	Power in the transmission line
V_1	Voltage of area 1
V_2	Voltage of area 2
δ_1	Phase angle of area 1
δ_2	Phase angle of area 2
X_{12}	Impedance of the transmission line
f	System frequency
ΔP_L	Instantaneous load changes
Δf_1	First area frequency change
Δf_2	Second area frequency change
Δf_{tie}	Connection point frequency change
N	Series cells per string
λ	Constant coefficient and depends upon the cell material
V_{PV}	Cell output voltage
I_{SC}	Cell short circuit current
I_{PV}	Cell output current
I_{PH}	Photocurrent
M	Parallel strings
I_0	Reverse saturation current
R_S	Series resistance of cell
a	negative value of zero in transfer function
b	Gain of PV system
c	Negative values of poles
d	Negative values of poles
K_{gov}	Governor gain
K_{tur}	Turbine gain

K_{reh}	Reheater gain
K_{ps}	Power system gain
T_{gov}	Governor time constant
T_{tur}	Turbine time constant
T_{reh}	Reheater time constant
T_{ps}	Power system time constant
P_{wt}	Wind turbine mechanical output power
ρ	Air density
a_s	Swept area
V	Wind speed
C_p	Rotor efficiency
TSR	Tip speed ratio
β	Pitch angle of the blade
ω_r	Rotor speed
D	Blade rotor diameter
K_{p1}	Pitch control gain
K_{p2}	Hydraulic pitch actuator gain
K_{p3}	Data fit pitch gain
K_{fc}	Fluid coupling gain
T_{p1}	Pitch control time constant
T_{p2}	Hydraulic pitch actuator time constant
T_{p3}	Data fit pitch time constant
T_w	Induction generator time constant
K_P	Proportional gain
K_D	Derivative gain
K_I	Integral gain
K_t	Tilt gain
K_{prd}	Predictive term constant
K_h	Delay time of the predictive term
n	Derivative action filter constant
λ	Fractional integrator order
t	Time
s	Second

Over the years, advancements in power systems have significantly increased their complexity compared to a century ago. Modern power systems operate at much higher power levels, making their control more challenging. The transition from megawatt (MW) to gigawatt (GW) power levels, the growing number and diversity of energy sources, the interconnection of regions through long transmission lines, unbalanced load distribution, voltage magnitude and phase differences between areas, fault conditions, and the integration of harmonic-generating systems such as electric vehicles have made power system operation increasingly complex[1].

Furthermore, the intermittent nature of renewable energy sources, such as solar and wind, adds to these challenges. Since their power generation depends on environmental conditions, the output fluctuates continuously. This variability poses significant difficulties in maintaining system stability and ensuring that loads receive voltage and power at the desired frequency and amplitude. Therefore, precise voltage and frequency control is essential both within individual generation areas and across interconnected regions[2,3].

In this study, automatic generation control (AGC), also referred to as load frequency control (LFC), is implemented in a two-area power system consisting of three different energy sources. Figure 1 illustrates the system structure, which integrates wind, solar, and thermal power generation.

In area-1, power is generated from solar energy, while area-2 consists of both wind and reheat-thermal power generation stations. The frequency deviation in area-1 is represented as Δf_1, while in area-2, it is denoted as Δf_2. The power deviation between the two areas is expressed as ΔP_{tie}. The generated power is supplied to various energy consumers, such as industrial facilities and residential loads.

Each power generation area is controlled independently. If a region is not connected to another system, it can operate autonomously. However, when different energy generation systems are interconnected within a grid, they must remain balanced with respect to each other. To achieve this balance, various controllers are employed. Commonly used controllers include proportional-integral (PI), proportional-integral-derivative (PID)[4], fractional order PID (FOPID)[5], fuzzy logic controllers (FLC)[6], and hybrid structures such as fuzzy logic integrated PID (FLPID) controllers[7,8]. The parameters of these controllers are typically tuned using different optimization algorithms. Several optimization techniques have been utilized, including the whale optimization algorithm (WOA)[9], the gray wolf optimizer (GWO)[10], genetic algorithm (GA) -based methods[11], JAYA algorithm[12], the water cycle algorithm (WCA)[13], and chaotic butterfly optimization[14]. Intelligent and adaptive control approaches have recently gained attention for improving renewable-based power system performance. Neural network controllers have been applied for battery storage regulation under varying load profiles[15], while hybrid energy management strategies integrating renewables and EV storage enhance grid flexibility[16]. Fuzzy-assisted sliding mode and neuro-fuzzy repetitive control frameworks further strengthen frequency and current regulation in modern microgrid and inverter systems[17,18].

To evaluate and compare the performance of the applied controllers, objective functions such as the integral of absolute error (IAE), integral of time-weighted absolute error (ITAE), integral of square error (ISE), and integral of time square error (ITSE) are employed[19]. Due to the practical challenges of experimental validation,

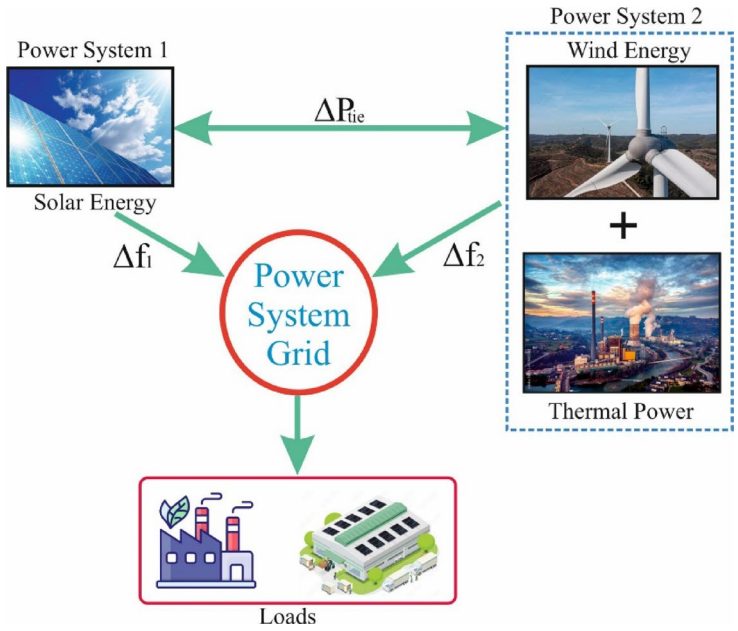

Fig. 1. Conceptual design for TAPS.

hardware platforms such as OPAL-RT have been developed. These devices enable experimental verification of simulation results and are highly effective in modeling power systems[20].

A more comprehensive literature review is presented in the next section.

Literature review

In the literature, various aspects of multi-area systems—including the number and types of regions, the types of controllers used, the optimization algorithms applied for controller parameter tuning, and the objective functions employed—are summarized in Table 1.

As seen in Table 1, various controllers have been employed in multi-area power systems, including conventional PID[21–23], PI-PD[24], high-order differential feedback controller (HODFC) and fractional high-order differential feedback controller (FHODFC)[25], series-connected controllers such as PI-PDN[26], tilt-integral-double derivative filter (TIDDF)[27], fractional order proportional integral derivative (FOPID)[28], fractional order proportional integral derivative-proportional resonant (FOPID-PR)[29], and 2DOFPID[30]; three-network double-delay actor-critic (TDAC)[31], FLC of type 1 and 2, as well as PID-tuned FLC[32], fractional order tilt-integral-derivative (FOTID)[33]; artificial neuro-fuzzy inference systems (ANFIS) and artificial neural networks (ANN)[34]; DOF-PDN, 2DOF-PDN, 3DOF-PDN, Neuro-Fuzzy 3DOF-PDN[23], and 3DOFPID-Fuzzy 3DOFPID[35].

Regarding optimization algorithms, various techniques have been employed, including modified moth swarm algorithm (mMSA)[21], GA, teaching learning-based optimization (TLBO)[22], particle swarm optimization (PSO)[25,26,34–36], crow search optimization algorithm (CSOA)[27], cuckoo optimization algorithm (COA) and COA integrated with the harmony search algorithm (HSCOA)[25], bear optimization algorithm (BOA), GWO[26], artificial hummingbird algorithm (AHB)[29], hybrid grey wolf optimization-pattern search (hGWO-PS)[30], deep reinforcement learning-based optimization and DWCA[32], search and rescue (SAR) Algorithm[33], ant colony optimization (ACO)[36], skill optimization algorithm (SOA)[23], coot optimization algorithm[28], moth flame optimizer (MFO), sine–cosine algorithm (SCA), salp swarm algorithm (SSA), PSO, ant-lion optimization algorithm (ALO)[37], big bang-big crunch (BB-BC) optimization, firebug swarm optimization (FSO), levenberg-marquardt algorithm (LMA), and PSO[35]. Additionally, numerous other optimization techniques have been explored in the literature.

The number of regions in the studies reviewed varies between two and five, with energy sources including thermal, photovoltaic, wind, hydro, and nuclear power. The number of energy generators in each region also differs depending on the system configuration.

Various controllers have been employed to regulate these systems. While PID-based controllers, different combinations of FOPID controllers, FLC, and DOFPID-based controllers are widely used, hybrid controllers such as Fuzzy-PID have also been commonly applied in load frequency control of multi-area power systems.

Finally, objective functions such as ITAE, IAE, ISE, and ITSE are frequently used for performance evaluation[21–42]. Among these, ITAE has been the most widely applied.

Motivation

The literature review indicates that various controllers and algorithms have been tested in different multi-area power system configurations, yet no definitive conclusion has been reached. Structural differences between systems lead to variations in controller parameters, making it necessary to design controllers specific to each

Year	Ref. no	Number of area/ energy unit	Type of energy production	Controller type	Optimization algorithm or method	Objective function
2024	[17]	5/10	Thermal Hydro/Thermal Wind/ Thermal Gas/ Hydro Diesel/ Hydro Wind	PID/FOFPID	mMSA	ITAE
2020	[18]	2/2	Non-reheat Thermal/Non-reheat Thermal	HODFC/FHODFC	PSO/COA/HSCOA	ITAE
		2/3	Re-Heat Thermal/Hydro/Gas			
2023	[19]	2/4	Thermal/Thermal	PI/PID	GA/PSO/TLBO	ITAE
2023	[20]	2/4	Non-reheat Steam Power/PV/ Non-reheat Steam Power/Wind	PI-PDN	GWO/PSO/BOA	ITAE
2024	[21]	2/2	Hydrothermal Power System/Hydrothermal Power System	TIDDF	CSOA	ISE
2024	[22]	5/10	Hydro/Wind/ Hydro/Diesel/ Diesel/Wind/ Hydro/Thermal/ Diesel/Thermal	FOPID-PR	AHB	ITAE
2023	[23]	2/2	Thermal/Thermal	2DOFPID	hGWO-PS	ITAE
2020	[24]	2/2	Hydro/Hydro	TDAC	Deep Reinforcement Learning Based TDAC	User Defined
2023	[25]	3/14	Multi Energy Production	Gaussian Interval-Based Type-2 Fuzzy PID Controller	Discrete Water Cycle Algorithm (DWCA)	ITAE
2024	[26]	2/6	Thermal/Hydro/Gas Thermal/Hydro/Gas	FOTID	SAR	ITAE
2023	[27]	2/2	Thermal/Thermal	ANFIS/ANN	PSO	ISE
2024	[28]	3/3	Thermal/Nuclear/Hydro	PID	GA/PSO/ACO	ITAE
2024	[29]	3/3	Thermal/Thermal/Thermal	DOF-PDN/ 2DOF-PDN/3DOF-PDN/ Neuro Fuzzy-3DOF-PDN	SOA	ISE
2023	[30]	2	Wind/PV	PID/FOPID	Coot Optimization Algorithm	ISE
2023	[31]	3/3	Reheat/Hydro/Gas	PI-PD	---	ISE/IAE/ITAE
2023	[32]	3/3	Non-Reheated Thermal/Non-Reheated Thermal	PID/FOPIDF/2DOFPID	MFO/SCA/ALO/SSA	ITAE
2024	[33]	3/6	Solar/Thermal Ocean/Termal & Nuclear Wind/Hydro	PID/Fuzzy 3DOFPID	BB-BC/LMA/FSO/PSO	ITSE
2021	[34]	3/3	Thermal/Thermal/Thermal + Flexible AC Transmission system	PDF + (1 + PI)	Grasshopper Optimization Algorithm	ITAE
2021	[35]	2/Multi-Microgrid	Thermal/Diesel Engine Generator/Micro Turbine/FC Fuel Cell/Photovoltaic/Wind Turbine/Battery/Flywheel Energy Storage System	Cascade PDF (1 + PI)	Imperialist Competitive Algorithm	ITAE
2022	[36]	1/Multi-DG (Microgrid)	PV/Wind/Diesel + EV/Battery	FO-T2F-PID	Improved Moth Swarm Algorithm	ISE
2021	[37]	2/4	Photovoltaic/Wind Turbine/HT Hydrothermal Unit/ Hydrogen Aqua Equalizer–Fuel Cell	Fractional-Order Fuzzy PID (FOFPID)	Sunflower Optimization	ITAE
2024	[38]	1/Multi-DG (Microgrid)	Solar/Wind/Diesel/Fuel Cell + Energy Storage Devices	F-TIDF-2	Improved Equilibrium Optimization	ISE

Table 1. A brief literature survey of multi-area power systems, controller type, and optimization algorithms.

system. This raises important questions regarding which controller should be selected and how its parameters should be determined.

Based on previous studies, it was considered important to choose a simple yet effective controller to achieve better results. This approach was expected to provide advantages in terms of settling time and maximum overshoot. Additionally, relatively new and less commonly used optimization algorithms were explored for parameter tuning. Finally, the aim was to validate the simulation results experimentally using the OPAL-RT OP5707 device.

Although numerous studies have applied various optimization algorithms and controllers for multi-area power systems, several limitations can still be observed. First, most existing research has primarily focused on conventional optimization algorithms such as PSO, GA, and GWO, while relatively few studies have explored newly emerging metaheuristic methods with enhanced convergence capability. Second, many studies concentrated only on simulation-based validation without real-time experimental verification, limiting their practical applicability. Third, most previous models considered systems with two homogeneous generation units, whereas highly renewable and hybrid configurations combining solar, wind, and thermal sources remain insufficiently explored.

These limitations motivate the present study, which addresses all of the above issues by (i) employing a novel optimization algorithm (FATA) with balanced exploration and exploitation mechanisms, (ii) validating the

results using an OPAL-RT real-time simulator, and (iii) considering a hybrid two-area system that integrates solar, wind, and thermal energy sources.

Contribution

The main contributions and novelties of this study are summarized as follows:

- A two-area highly renewable hybrid power system, integrating solar, wind, and thermal generation units, was considered and analyzed for the LFC problem.
- The study introduces a novel application of the FATA for optimizing AGC parameters. To the best of our knowledge, this is the first implementation of FATA validated through a real-time simulation load frequency control using the OPAL-RT platform.
- A comprehensive comparative framework was designed, combining four controller types (PI, PIDn, FOPI, and PPIDn) with four optimization algorithms (GJO, ECO, ESC, and FATA) to identify the most effective configuration for frequency stabilization.
- The proposed approach was experimentally validated on the OPAL-RT OP5707 real-time simulator, demonstrating its practical feasibility and robustness under realistic operating conditions.

Article organization

This article consists of five sections. The first section includes the Introduction, Literature Review, and Motivation, followed by the Article Organization. In the second section, information is provided on multi-area power systems, the controllers used for their regulation, and the applied optimization algorithms. The third section presents simulation studies and experimental results. The fourth section analyzes the obtained results, while the final section provides a general evaluation of the study and its findings. Additionally, recommendations are offered to guide future research.

Figure 2 illustrates the organizational structure of the article.

Problem formulation

Figure 3 illustrates a two-area power system incorporating three different energy generation sources: solar, thermal, and wind. The system has been controlled using four different controllers (PI, PIDn, FOPI, and PPIDn). To optimize the parameters of each controller, four optimization algorithms (GJO, ECO, ESC, and FATA) were applied. The objective was to determine the most effective combination of controller and optimization algorithm for achieving optimal system performance.

The optimization algorithms adjusted the controller parameters based on the ITAE criterion, which is widely used in the literature for evaluating control performance. By minimizing ITAE, the controllers were fine-tuned to enhance system stability and dynamic response. The overall structure of the system, along with the interaction between controllers, energy sources, and optimization methods, is schematically presented in Fig. 3.

Two-area power system (TAPS)

In a two-area power system, the power transmitted through the transmission line is given by Eq. (1).

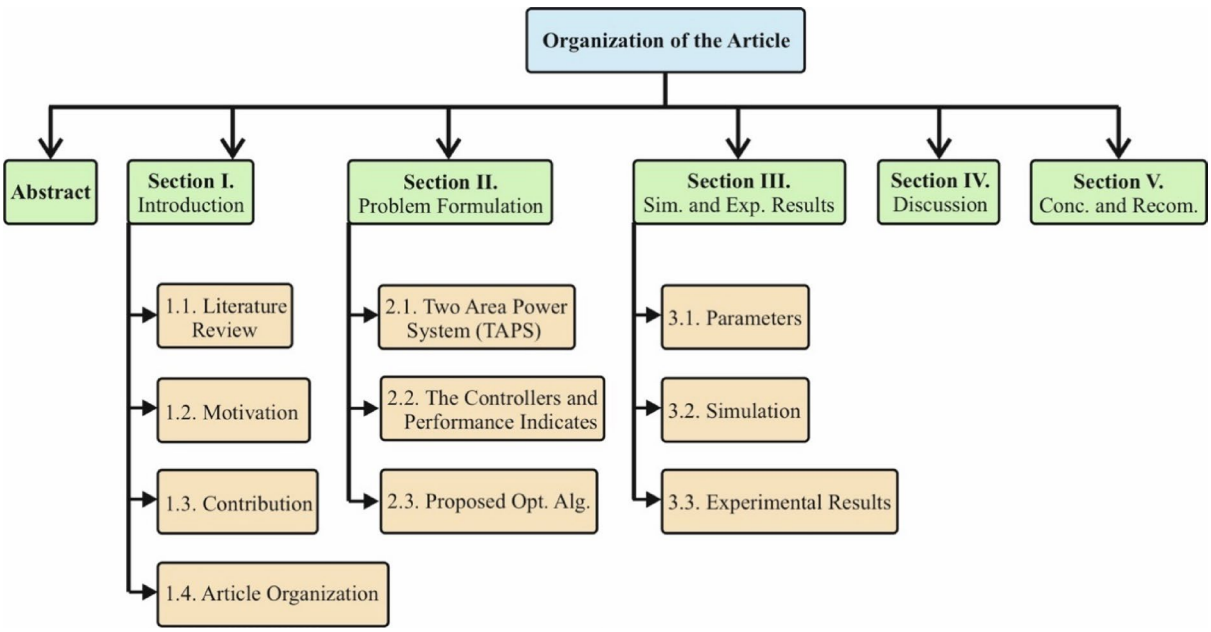

Fig. 2. Organization of the paper.

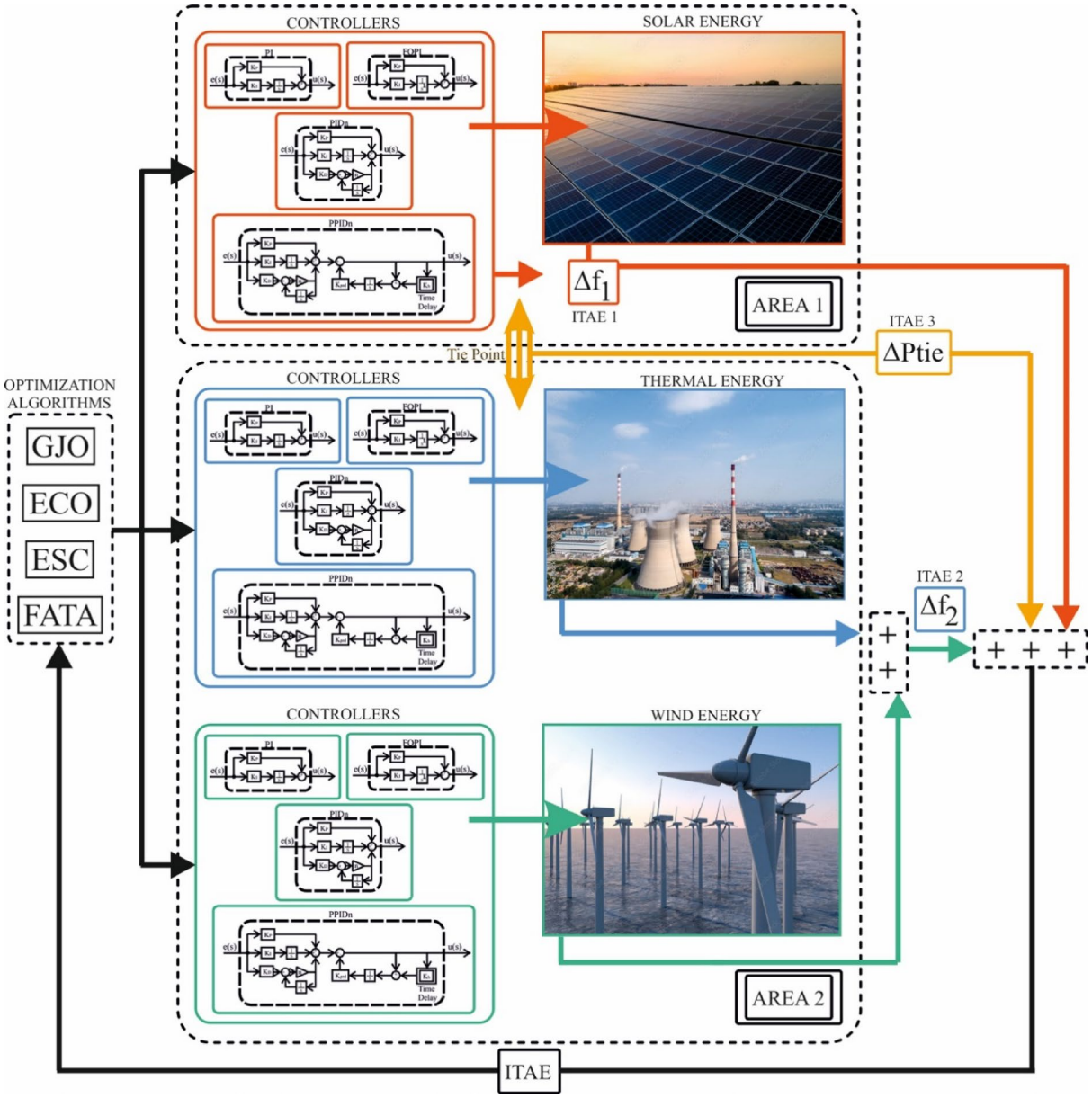

Fig. 3. Two-area three power generation units power system and controller optimization.

$$P_{line12} = \frac{|V_1| . |V_2|}{X_{12}} \sin(\delta_1 - \delta_2) \tag{1}$$

In this equation, V_1 (V) and V_2 (V) represent the voltages of area-1 and area-2, respectively, while δ_1 (^{0}) and δ_2 (^{0}) correspond to their phase angles. The term P_{line12} denotes the power flow through the transmission line, and X_{12} represents the line impedance.

The rate of change of the phase angle in each area is given by Eq. (2), where f (Hz) represents the system frequency.

$$\Delta\delta = 2\pi \int \Delta f dt \tag{2}$$

$$\Delta P_{12} = \frac{|V_1| . |V_2|}{X_{12}} \cos(\delta_1 - \delta_2)(\Delta\delta_1 - \Delta\delta_2) = T_{12}(\Delta\delta_1 - \Delta\delta_2) \tag{3}$$

$$T_{12} = \frac{|V_1| . |V_2|}{X_{12}} \cos(\delta_1 - \delta_2) \tag{4}$$

$$\Delta P_{tie} = T_{12}(\Delta\delta_1 - \Delta\delta_2) \tag{5}$$

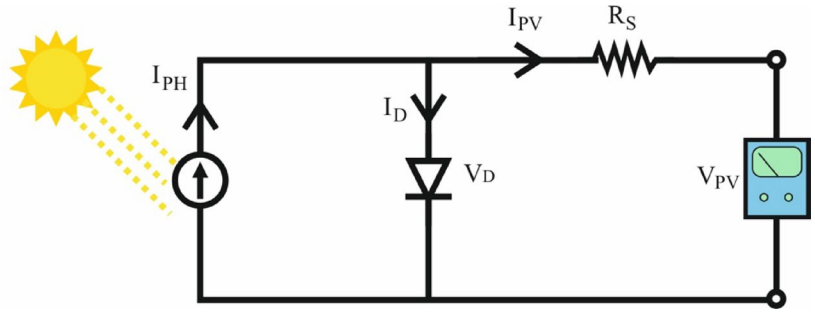

Fig. 4. Solar cell equivalent circuit.

Expression		Definition	Unit
N	:	Series cells per string	
λ	:	Constant coefficient and depends upon the cell material	
V_{PV}	:	Cell output voltage	V
I_{SC}	:	Cell short circuit current	A
I_{PV}	:	Cell output current	A
I_{PH}	:	Photocurrent	A
M	:	Parallel strings	
I_0	:	Reverse saturation current	A
R_S	:	Series resistance of cell	Ω

Table 2. The descriptions for PV cell.

The exchange of power between the regions is represented by Eq. (3), while the synchronizing torque coefficient is formulated in Eq. (4). The variation in power flow through the transmission line is expressed in Eq. (5). Instantaneous load fluctuations (ΔP_L) lead to frequency deviations in the system. Consequently, the power variation and the Area Control Error (ACE) are mathematically defined in Eqs. (6) and (7), where B denotes the frequency bias factor[1,3].

$$ACE_1 = -B\Delta f_1 - \Delta P_{tie} \tag{6}$$

$$ACE_2 = -B\Delta f_2 + \Delta P_{tie} \tag{7}$$

The obtained values represent the error signals at the input of the controllers.

The TAPS system consists of three different energy generation units: a solar power system composed of photovoltaic (PV) panels, a thermal power generation station, and wind energy produced by wind turbines. The photovoltaic solar system constitutes area-1, while the thermal power station and wind turbines together form area-2.

In area-1, photovoltaic solar panels are semiconductor devices that convert sunlight into electrical energy. Figure 4 illustrates a simplified equivalent circuit of a solar cell. Equation (8) expresses the voltage generated by a solar cell. By connecting multiple solar cells in series and parallel, solar panels are formed[43,44].

$$V_{PV} = \frac{N}{\lambda} ln\left(\frac{I_{SC} - I_{PV} + MI_0}{MI_0}\right) - \frac{N}{M} R_s I_{PV} \tag{8}$$

The definitions and units of the PV variables are presented in Table 2.

The transfer function of the power generation system composed of solar panels is given in Eq. (9). This transfer function represents the overall dynamics of the inverter, filters, and maximum power point tracking (MPPT) system.

$$\text{PV System}: \; G_{PV}(s) = \frac{a + bs}{s^2 + cs + d} \tag{9}$$

where a corresponds to the negative value of the system's zero, c and d represent the negative values of the poles, and b denotes the gain of the PV system[45,46].

In area-2, two different power generation units are present: a thermal power plant and a wind energy system. The transfer functions of the thermal power system components, including the governor, reheat system, turbine, and power system, are expressed in Equations (10) to (13).

Expression		Definition	Unit
K_{gov}	:	Governor gain	p.u.
K_{tur}	:	Turbine gain	p.u.
K_{reh}	:	Reheater gain	p.u.
K_{ps}	:	Power system gain	p.u.
T_{gov}	:	Governor time constant	s
T_{tur}	:	Turbine time constant	s
T_{reh}	:	Reheater time constant	s
T_{ps}	:	Power system time constant	s

Table 3. The descriptions for thermal energy production unit.

Expression		Definition	Unit
P_{wt}	:	Wind turbine mechanical output power	W
ρ	:	Air density	Kg/m^3
a_s	:	Swept area	m^2
V	:	Wind speed	m/s
C_p	:	Rotor efficiency	
TSR	:	Tip speed ratio	
β	:	Pitch angle of the blade	Degree
ω_r	:	Rotor speed	rad/s
D	:	Blade rotor diameter	m

Table 4. Wind energy parameters.

$$\text{Governor}: \ G_{gov}(s) = \frac{K_{gov}}{sT_{gov}+1} \tag{10}$$

$$\text{Turbine}: \ G_{tur}(s) = \frac{K_{tur}}{sT_{tur}+1} \tag{11}$$

$$\text{Reheater}: \ G_{reh}(s) = \frac{sK_{reh}T_{reh}+1}{sT_p+1} \tag{12}$$

$$\text{Power System}: \ G_{PS}(s) = \frac{K_{PS}}{sT_{PS}+1} \tag{13}$$

Table 3 provides definitions for the parameters used in the transfer functions of the thermal power system components, including the governor, reheater, turbine, and power system.

The second power generation system in area-2 is the wind energy system. Wind turbines harness the kinetic energy of the wind to rotate their blades. The rotor is connected to a shaft that drives a generator operating in motor-generator mode, converting mechanical energy into electrical power[47].

The mathematical representation of the output power generated by a wind turbine is given in Equations (14) to (16).

$$P_{wt} = \frac{1}{2}\rho\, a_s^2 V^3 C_p\,(TSR, \beta\,) \tag{14}$$

$$C_p = \left(TSR - 0.022\beta^{\,2} - 5.6\right) e^{-0.17TSR} \tag{15}$$

$$TSR = \frac{w_r.\pi\, D}{60V} \tag{16}$$

The definitions of the terms used in the equations are provided in Table 4.

Based on these fundamental equations, the transfer functions of the wind turbine components have been derived and are presented in Equations (17) to (21)[48].

$$\text{Pitch Control}: \ G_{pc}(s) = \frac{K_{p1}(sT_{p1}+1)}{s+1} \tag{17}$$

$$\text{Hydraulic Pitch Actuator}: \ G_{hpa}(s) = \frac{K_{p2}}{sT_{p2}+1} \tag{18}$$

Expression		Definition	Unit
K_{p1}	:	Pitch control gain	p.u.
K_{p2}	:	Hydraulic pitch actuator gain	p.u.
K_{p3}	:	Data fit pitch gain	p.u.
K_{fc}	:	Fluid coupling gain	p.u.
T_{p1}	:	Pitch control time constant	s
T_{p2}	:	Hydraulic pitch actuator time constant	s
T_{p3}	:	Data fit pitch time constant	s
T_w	:	Induction generator time constant	s

Table 5. Descriptions and units of the variables used in the transfer functions.

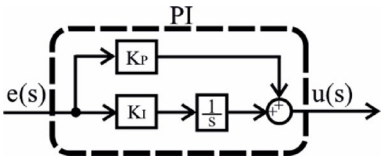

Fig. 5. PI controller.

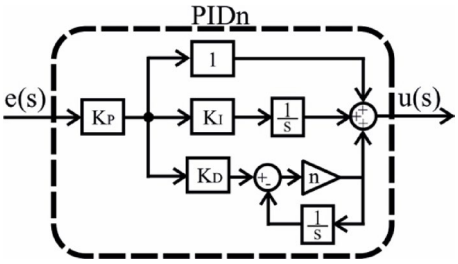

Fig. 6. PIDn controller.

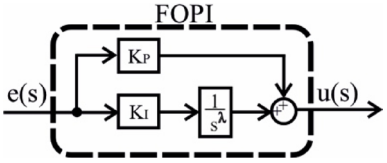

Fig. 7. FOPI controller.

$$\text{Data Fit Pitch}: \; G_{dfp}(s) = \frac{K_{p3}}{sT_{p3}+1} \tag{19}$$

$$\text{Induction Generator}: \; G_{IG}(s) = \frac{1}{sT_w+1} \tag{20}$$

$$\text{Output Wind Power Deviation}: \; \Delta P_{wt}(s) = K_{fc}G_{IG}(s) \tag{21}$$

The descriptions of the equations used in Equations (17) to (21) are provided in Table 5.

The controllers and performance indices

In this study, four different controllers were selected and their parameters were optimized. The selection was based on a comprehensive literature review, focusing on controllers expected to exhibit high performance. As a result, PI, PIDn, FOPI, and PPIDn controllers were chosen. The structural representations of these controllers are illustrated in Figs. 5, 6, 7 and 8, while their mathematical formulations are provided in Equations (22) to (25) where the ideal connection forms of the PIDn and PPIDn controllers are performed.

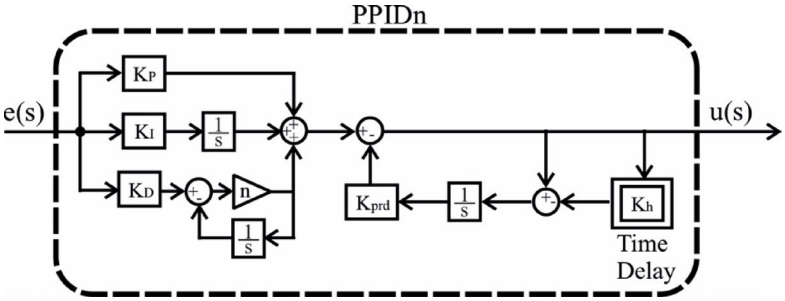

Fig. 8. PPIDn controller.

Expression		Definition
K_p	:	Proportional gain
K_D	:	Derivative gain
K_I	:	Integral gain
K_{prd}	:	Predictive term constant
K_h	:	Delay time of the predictive term
n	:	Derivative action filter constant
λ		Fractional integrator order

Table 6. The controller parameters.

$$\frac{u(s)}{e(s)} = G_{PID} = K_P + \frac{K_I}{s} \tag{22}$$

$$\frac{u(s)}{e(s)} = G_{PIDn} = K_P\left(1 + \frac{K_I}{s} + K_D\left(\frac{ns}{s+n}\right)\right) \tag{23}$$

$$\frac{u(s)}{e(s)} = G_{FOPID} = K_P + \frac{K_I}{s^{\lambda}} \tag{24}$$

$$U(s) = \left(K_p + \frac{K_I}{s} + sK_D\frac{n}{s+n}\right)E(s) - \frac{K_{prd}}{s}\left(1 - e^{-sK_h}\right)U(s) \tag{25}$$

The descriptions of the terms used in Equations (22) to (25) are provided in Table 6.

To compare the performance of the controllers, error performance indices, as defined in Equations (26) to (29), were utilized. This approach is consistent with findings from the literature review. Typically, one of these indices is selected to evaluate control performance. In this study, ITAE was chosen due to its widespread use.

$$\mathrm{ISE} = \int_0^{\infty} \mathrm{e}^2(\mathrm{t})\,\mathrm{dt} \tag{26}$$

$$\mathrm{IAE} = \int_0^{\infty} |\mathrm{e}(\mathrm{t})|\,\mathrm{dt} \tag{27}$$

$$\mathrm{ITSE} = \int_0^{\infty} \mathrm{te}^2(\mathrm{t})\,\mathrm{dt} \tag{28}$$

$$\mathrm{ITAE} = \int_0^{\infty} \mathrm{t}\,|\mathrm{e}(\mathrm{t})|\,\mathrm{dt} \tag{29}$$

Another reason to employ ITAE is that it provides a balanced trade-off between transient and steady-state responses. In LFC, long-term deviations are often more critical than short-term overshoots. Therefore, the time-weighting factor in ITAE effectively penalizes prolonged oscillations while ensuring faster settling with minimal steady-state error. This makes ITAE a more appropriate index for evaluating controller performance in interconnected power systems compared to other popular indices such as ISE, IAE, and ITSE.

In the simulation, the objective function, presented in Eq. (30), was derived from the sum of the errors in each region and the interconnection point. The optimization algorithms were then evaluated based on this criterion. (st: simulation time)

$$OF_{ITAE} = \int_0^{st} t\,|\Delta_{f1}|\,dt + \int_0^{st} t\,|\Delta_{f2}|\,dt + \int_0^{st} t\,|\Delta_{Ptie}|\,dt \tag{30}$$

In this equation, Eq. (29) was applied based on the frequency deviations in each region and at the interconnection point[49,50].

Proposed optimization algorithm

In this study, the parameters of four different controllers (PI, PIDn, FOPI, and PPIDn) were optimized using four optimization algorithms: GJO, ECO, ESC, and FATA. Each algorithm was selected based on its potential effectiveness in optimizing control parameters. A comparative analysis was conducted to evaluate their performance, with a particular emphasis on the FATA algorithm, which demonstrated superior results in this context.

Overview of the FATA

The Fata Morgana Algorithm (FATA) is a newly developed optimization technique inspired by the Fata Morgana optical phenomenon, a complex mirage effect caused by atmospheric refraction. This phenomenon creates illusions of floating landscapes or distorted images due to variations in air density and light refraction. By mimicking these principles, the FATA algorithm introduces a novel approach to balancing global exploration and local exploitation in optimization tasks.

Unlike conventional metaheuristic algorithms that rely on predefined search mechanisms, FATA dynamically adjusts its search behavior through two key principles:

1. The mirage light filtering principle, which selectively refines the population based on an integral-based evaluation method, enhancing solution quality.
2. The light propagation principle, which governs the movement and adaptation of solutions, ensuring efficient exploration and convergence.

By integrating these mechanisms, FATA provides a robust framework for solving complex optimization problems, effectively avoiding local optima while maintaining convergence efficiency. The following sections detail the inspiration behind FATA, its mathematical formulation, and its application in controller optimization.

Inspiration behind the Fata Morgana phenomenon

The fata morgana, or mirage, is a naturally occurring optical phenomenon. It arises due to the behavior of light as it propagates through an atmosphere with varying density, transitioning from an optically denser medium to a less dense one. This study investigates the formation of mirages by examining light rays emitted from underwater features. It also inspires the design depicted in Fig. 9. The figure demonstrates the optical path of light rays emitted from a ship at sea, which ultimately create a mirage. The formation of a mirage necessitates two conditions: a medium with non-uniform density and the propagation of light through this medium. Initially, solar heating induces temperature variations in the atmosphere, creating the required inhomogeneous density gradient. When light from the ship reflects into this medium, its refraction angle continuously changes during

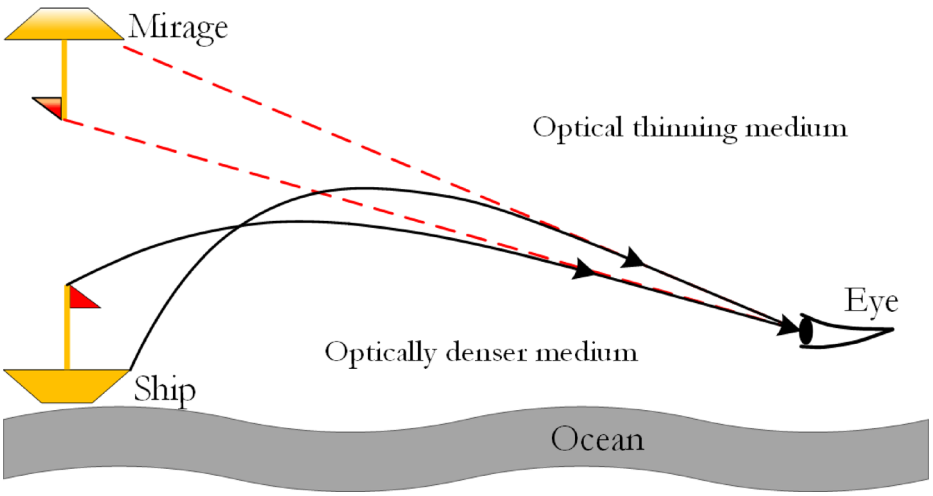

Fig. 9. Mirage Formation Process[51].

propagation, culminating in total internal reflection, which produces the mirage effect. An observer (as shown by the Eye in Fig. 9) perceives this phenomenon when looking towards the sky in a specific direction (red)[51].

As illustrated in Fig. 9, the formation of a mirage depends on the delicate balance between filtering mirage light and managing light refraction and reflection during propagation. Similarly, a parallel can be drawn to swarm intelligence algorithms, where achieving a balance between global exploration and local exploitation remains a challenge. Current algorithms, such as the Harris Hawks Optimization (HHO), sequentially implement global and local search strategies, using soft and hard besiege mechanisms inspired by hawk hunting. However, these strategies often lack the fine balance observed in the mirage phenomenon.

The mirage principle, illustrated in Fig. 9, offers an innovative approach to algorithm design by harmonizing global and local search strategies. In this figure, light emitted by a ship enters an atmosphere with a non-uniform density. As it transitions from an optically denser medium to a less dense one, the refractive index changes, causing the light to bend at progressively larger angles. Upon reaching the critical angle, total internal reflection occurs, resulting in the formation of a mirage. This dynamic balance between refraction and reflection processes serves as the conceptual foundation for a new optimization framework.

Building upon this concept, the paper introduces two key principles essential to the proposed FATA: the mirage light filtering principle and the light propagation principle. The former governs the selection process, allowing specific light waves to contribute to the mirage while excluding others, whereas the latter dictates how light adjusts its direction and intensity as it travels through a medium with varying density. These principles play a crucial role in shaping the behavior of swarm intelligence algorithms.

The FATA algorithm derives its global search strategy (mirage light filtering principle) from the light reflected by the ship into the medium, while its local search strategy (light propagation principle) is inspired by the refraction and total internal reflection of light. Together, these principles form the core of the algorithm, achieving a balance between exploration and exploitation.

By emulating the mirage formation process, FATA integrates these strategies seamlessly, creating a robust optimization framework. This alignment between the optical phenomenon and the algorithm's design ensures consistency and effectiveness, establishing the FATA as a novel and balanced optimization tool.

Fata Morgana algorithm

As depicted in Fig. 10, the FATA represents the population as multiple light rays that contribute to forming a mirage, with each light ray (x) representing an individual within the population. The mirage (x_{best}) serves as the optimization target.

At the initial stage, the population of light rays undergoes a dynamic assessment based on the mirage light filtering principle, which is rooted in the definite integral concept. This process evaluates the light emitted from the hull, specifically located in the lower-left corner of Fig. 10. Within this population, some light rays undergo physical transformations to form the mirage (x_{best}), while others, though similarly transformed, propagate in directions that do not contribute to forming the mirage.

In the second stage, the filtered light population undergoes the light propagation strategy, encompassing processes of refraction in the first and second stages and total internal reflection. The propagation of light through a medium with an inhomogeneous density mirrors the exchange of information between individuals in the algorithm. Through this process, the algorithm iteratively explores the solution space, leveraging physical changes in light propagation to identify the target mirage (x_{best}), which corresponds to the optimal solution[51].

The Mirage light filtering principle This section outlines the population search mechanism of FATA, drawing inspiration from the definite integral principle. As shown in Fig. 10, the hull emits two different types of light

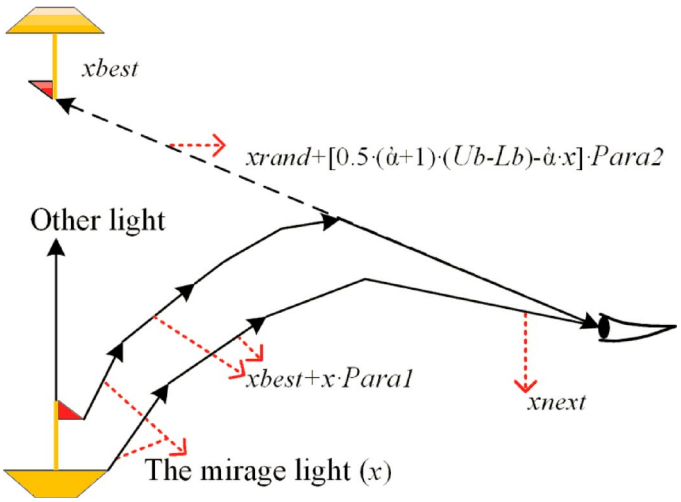

Fig. 10. FATA optimization process in three dimensions[51].

rays during the mirage formation process. The first type, labeled as 'other light' in Fig. 10, plays no role in forming the mirage and dissipates without undergoing notable changes. The second type, termed "mirage light (x)," undergoes physical changes, ultimately forming the mirage[51].

In FATA, differentiating between these two light populations is essential to identifying the optimal solution, x_{best}. To achieve this, FATA adopts a population quality evaluation mechanism grounded in the principle of definite integrals, enabling effective distinction and selection of relevant populations. Analogous to swarm intelligence algorithms, the quality of a population is measured by aggregating the fitness of individuals within it. As shown in Fig. 11a, ranking the fitness of individuals in a population creates a cumulative curve. To streamline the fitness computation of the two types of light populations ("other light" and "mirage light"), FATA applies definite integration to evaluate the area under this curve (Fig. 11b). The resulting integral value serves as an indicator of population fitness. Using this approach, FATA isolates the filtered mirage light population, which represents individuals selected based on their integral-based fitness evaluation.

This method enables FATA to efficiently balance exploration and exploitation by focusing on high-quality populations, ensuring robust optimization performance.

The FATA employs a fitness evaluation strategy to classify the population into two categories: "other light" and "mirage light," based on population quality. The population quality refers to the overall performance or effectiveness of the population. In this strategy, the integrated area (S) under the population fitness function ($f(x)$) curve is used as a measure of population quality. Figure 11a illustrates the curve representing the population fitness function, while Fig. 11b depicts the integrated area (S) beneath this curve.

In swarm intelligence algorithms (SIAs), fitness typically represents the quality of individual solutions. However, evaluating the overall population quality becomes challenging when fitness values are discrete and high-dimensional. To address this, individual fitness values are approximated using a continuous function ($f(x)$). The FATA leverages the principle of definite integration to compute the integrated area (S) of the population fitness function curve. This integrated area serves as a comprehensive metric to assess and compare the quality of different populations.

By quantifying population quality through definite integration, FATA ensures an efficient and reliable mechanism for distinguishing high-quality populations, enabling the application of appropriate search strategies tailored to either the "other light" or "mirage light" populations[51].

$$x_i^{next} = \begin{cases} L_b + (U_b - L_b) \bullet rand & , rand > P \\ x_{best} + x_i \bullet Para_1 & , rand \leq P \ and \ rand < q \\ x_{rand} + [0.5 \bullet (\alpha + 1)(U_b - L_b) - \alpha x_i] \bullet Para_2 & , rand \leq P \ and \ rand \geq q \end{cases} \tag{31}$$

$$P = \frac{S - S_{worst}}{S_{best} - S_{worst}} \tag{32}$$

$$q = \frac{fit_i - fit_{worst}}{fit_{best} - fit_{worst}} \tag{33}$$

In the FATA, x represents an individual light, while x^{next} denotes the new individual generated during the optimization process. Algorithm 1 outlines the mirage light filtering principle employed by FATA. This filtering process includes three primary strategies: the first-half refraction strategy, the second-half refraction strategy, and the total internal reflection strategy, which are detailed sequentially in Sect. 3.2.

The population quality factor (P) is defined in Eq. (31), where a smaller value of the integrated area (S) indicates a higher-quality population. Specifically, S_{worst} and S_{best} represent the quality of the worst and best populations, respectively. Populations classified as mirage light populations exhibit superior quality, characterized by smaller S values.

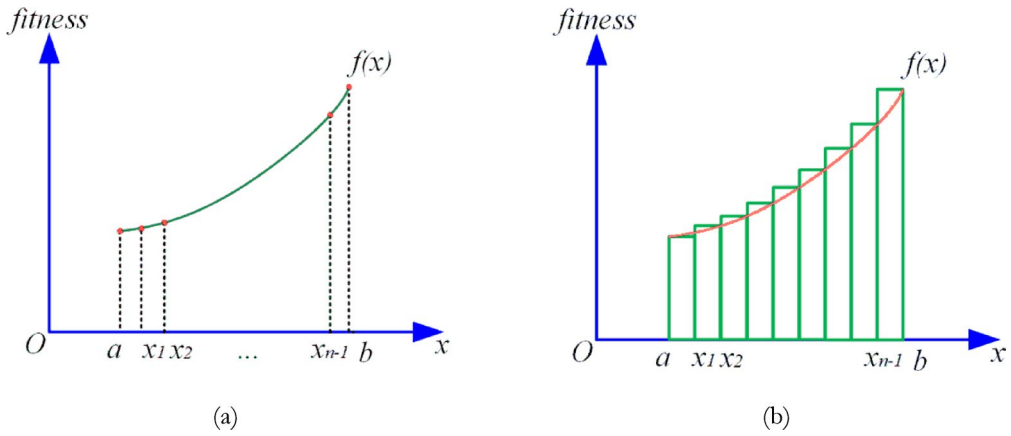

Fig. 11. Population fitness curve in FATA (**a**) Population fitness function curve (**b**) Integrated area (S) Under the curve[51].

In Eq. (31), the individual quality factor (q) is introduced, which quantifies the performance of each individual within the population. Here, fit_i represents the fitness of the current individual (x), fit_{worst} corresponds to the fitness of the worst-performing individual, and fit_{best} represents the fitness of the best individual. By leveraging these fitness metrics and quality factors, FATA effectively identifies and prioritizes high-performing mirage light populations and individuals to guide the optimization process[51].

Input: light individual x;

Fit the population quality function $f(x)$ according to the fitness of the individuals;

Calculate the integrated area S of the $f(x)$ based on the principle of definite integration;

Update the optimal area S_{best} and the worst area S_{worst} ;

Calculate the population quality factor P by Eq. (32);

If $rand > P$

The population is the light rays directed towards a medium with inhomogeneous density populations;

The population performs Eq. (31) to initialize the population randomly;

Else

The population is the light rays not directed towards a medium with inhomogeneous density populations;

The population executes the search strategy (Eqs. (31));

End If

Return new individual x^{next} ;

Algorithm 1. The mirage light filtering strategy

$$y = f(x) = \sum {}_{j=0}^{n} c_j \phi_j x \tag{34}$$

$$S = \int_a^b f(x)\,dx \approx \frac{b-a}{n} \bullet \left(\frac{y_0 + y_1}{2} + \frac{y_1 + y_2}{2} + \ldots + \frac{y_{n-1} + y_n}{2}\right) \tag{35}$$

Equations (34–35) detail the process of calculating the area (S) under the population fitness curve $f(x)$ ($f(x_1) < f(x_2) \ldots < f(x_i) \ldots < f(x_n)$) using the principle of definite integration. This principle leverages the concept of limits to compute the integrated area of $f(x)$. Specifically, Eq. (34) defines the population quality fitting function $f(x)$, which represents the fitness curve using discrete points (x_i, y_i), where $i \in [1, n]$. The parameters c_j and ϕ_j are used within the fitting function to optimize the representation of the curve. This approach ensures accurate estimation of population quality by evaluating the overall fitness distribution within the population.

Light propagation principle In FATA, the light propagation principle is applied following the mirage light filtering strategy. This mechanism functions as the algorithm's local search approach, enhancing exploitation within the search space to identify minima. As shown in Fig. 12, the mirage light rays in FATA originate from a small boat positioned in the lower-left corner of the search space.

Initially, the light population undergoes the mirage light filtering process, where the population is evaluated and refined using calculus-based principles to identify individuals contributing to the mirage phenomenon. After this filtering, the refined mirage light population is subjected to sequential refraction and reflection processes. During these stages, the direction and size of the light rays adapt dynamically, as depicted in Fig. 12, showcasing their transformations. This iterative procedure allows the filtered light population to explore the local search space effectively, optimizing the chances of locating a local minimum.

FATA employs a distinct search strategy based on the light propagation principle, further refined using trigonometric functions. This approach consists of three sequential components: the refraction strategy in the initial phase, the reflection strategy in the subsequent phase, and a final refraction step. The application of these strategies is governed by the individual quality factor defined in Eq. (35).

Light Refraction (First Half Phase): In this phase, illustrated in Figure 13, light rays (denoted as x) enter a medium with varying density, transitioning from an optically denser medium to a less dense medium. During this transition, both the direction and size of the light rays are altered. The relationship between the angle of incidence (i_1) and the angle of refraction (i_2) follows the principle that $i_1 < i_2$.

Figure 13 visually analyzes the process of refraction for the light individuals. The light ray is represented as x, and the refractive surface is labeled as the level. After undergoing the first half of the refraction process, a new individual,), x^{next}, is generated, as defined by Eq. (36). The relationship $NO = C \bullet OM$, where C is

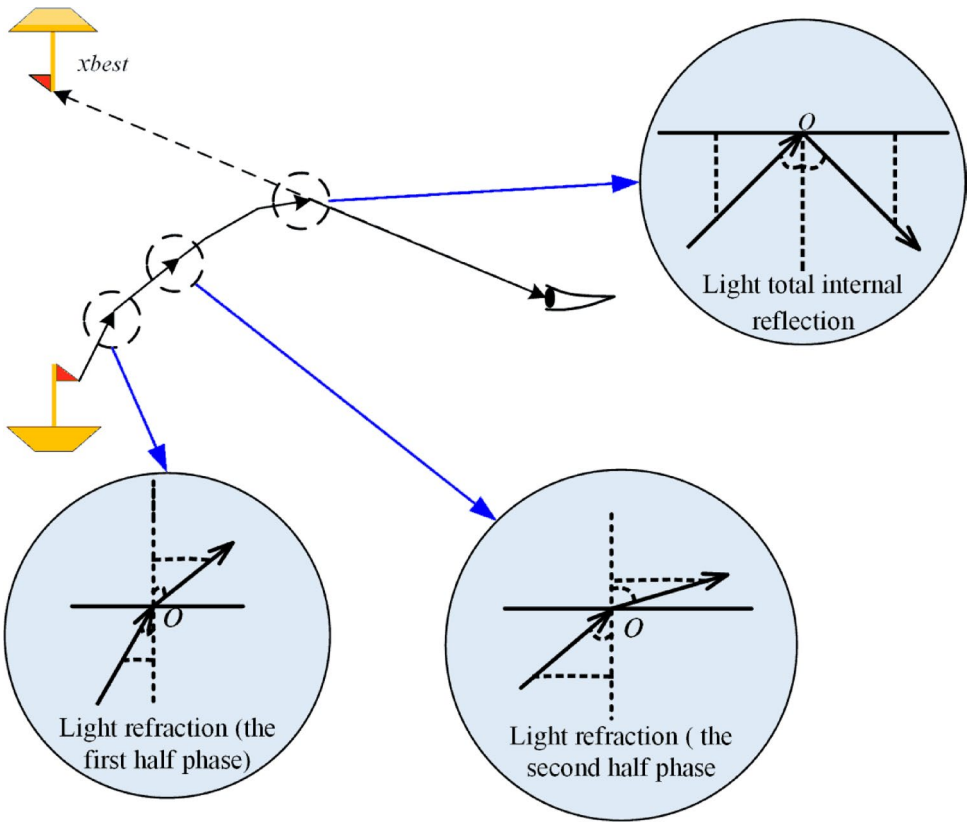

Fig. 12. FATA algorithm and the mirage principle[51].

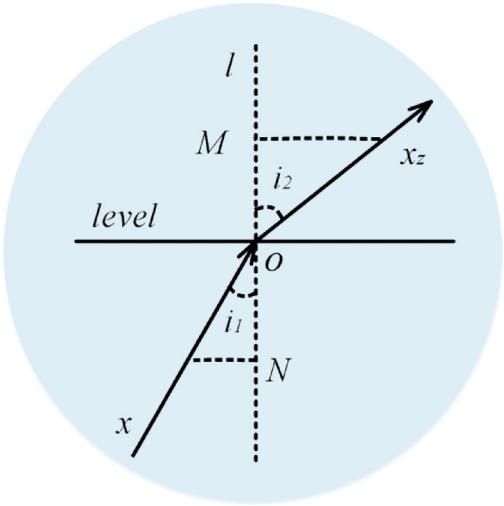

Fig. 13. First refraction process of light.

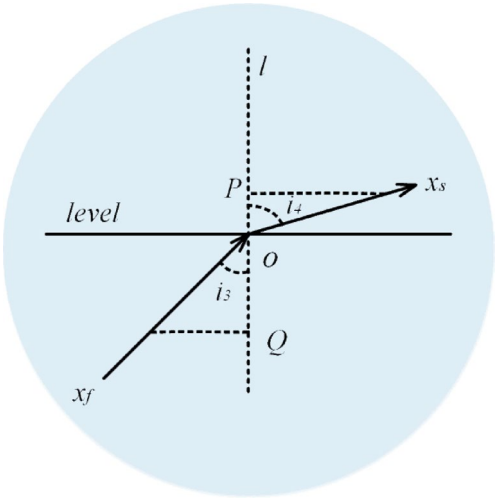

Fig. 14. Second refraction process of light.

a constant, is assumed for this phase. The equations (Eqs. 36–38) govern the transformations in this strategy, guiding the propagation of light rays through the medium.

$$x^{next} = x_{best} + x_z \tag{36}$$

$$x_z = x \bullet Para_1 \tag{37}$$

$$Para_1 = \frac{\sin(i_1)}{C \bullet \cos(i_2)} = \tan(\theta) \tag{38}$$

In the FATA, the propagation of light individuals involves dynamic adjustments during the first-half refraction strategy. Here, x^{next} denotes the newly generated individual, while x_{best} represents the current best individual. The refraction step is symbolized as x_z, which describes the intermediate adjustment of the individual during the refraction process.

A key parameter in this strategy is $Para_1$, the first-half refraction ratio, which dynamically changes during light propagation. This parameter regulates the degree of transformation the light individual undergoes when passing from one medium to another.

To simplify the measurement of the incident angle (i_1) and the refraction angle (i_2), the algorithm introduces the parameter θ, which substitutes the angle variation. In the algorithm, θ is defined within the range $[0,1]$, providing a normalized and efficient means to represent the angle change during the refraction process. Equation (38) encapsulates this relationship, ensuring accurate computation of the transformations during light propagation[51].

Light Refraction (Second Half Phase): Following the first half refraction phase, the light enters the second half refraction phase, where it propagates through random points within the medium. As illustrated in Fig. 14, the process is characterized by the angle of incidence (i_3) being smaller than the angle of refraction (i_4). This occurs because the light travels through a medium with varying density, resulting in a continuously changing refractive index ($Para_2$).

During this phase, the light individual (x_f) generates a new individual (x^{next}) by incorporating information from random individuals (x_{rand}) located within the search space. This random selection enhances the exploration capabilities of the algorithm. The transformations involved in this refraction process are mathematically described in Eqs. (41–43), which outline the systematic generation of new individuals in the context of FATA's refraction strategy.

$$x^{next} = x_{rand} + x_s \tag{39}$$

$$x_s = x_f \bullet Para_2 \tag{40}$$

$$Para_2 = \frac{cos\,(i_5)}{C \bullet sin\,(i_6)} = \frac{1}{tan\,(\theta\,)} \tag{41}$$

In the second half refraction strategy, x_s represents the refraction step, while x_{rand} denotes a randomly selected individual from the population. The second refraction ratio, $Para_2$, plays a key role in determining the behavior of light propagation during this phase.

As illustrated in Fig. 15a, the value of $Para_1$ oscillates randomly within the range $[-2,2]$ and converges toward zero as the number of iterations increases. Conversely, Fig. 15b shows that $Para_2$ exhibits random oscillations between [−150,150], with a general upward trend as iterations progress.

It is observed that both parameters initially have large values. To enhance the algorithm's efficiency, these parameters are scaled to the standardized interval $[0,1]$. The oscillatory nature of $Para_2$, particularly in the later stages of the FATA, improves its ability to escape local optima, thereby enhancing the robustness of the search process. Standardizing these parameters ensures smoother progression and better performance in optimization tasks.

The total internal reflection phase marks the culmination of the light propagation process in the formation of the mirage phenomenon. This stage occurs when the angle of refraction reaches a threshold where further refraction becomes impossible, causing the light to reflect entirely within the medium of inhomogeneous density.

This principle is implemented in the FATA as a total internal reflection strategy, which encourages the population to explore in the opposite direction, thereby enhancing diversity and exploration. As shown in Fig. 16, the angle of incidence (i_5) equals the angle of reflection (i_6), adhering to the laws of reflection.

In the Fig. 16:

- $O\,(x_0, 0)$ denotes the center point of the interval ($[L_b, U_b]$)., where L_b and U_b represent the lower and upper bounds of the search space.
- E and F represent the vertical distances of the incident and refracted light rays from the horizontal plane, respectively.

The total internal reflection strategy modifies the light individual (x) into a new individual (x^{next}) that explores the search space in the reverse direction. This mechanism increases the algorithm's ability to identify global

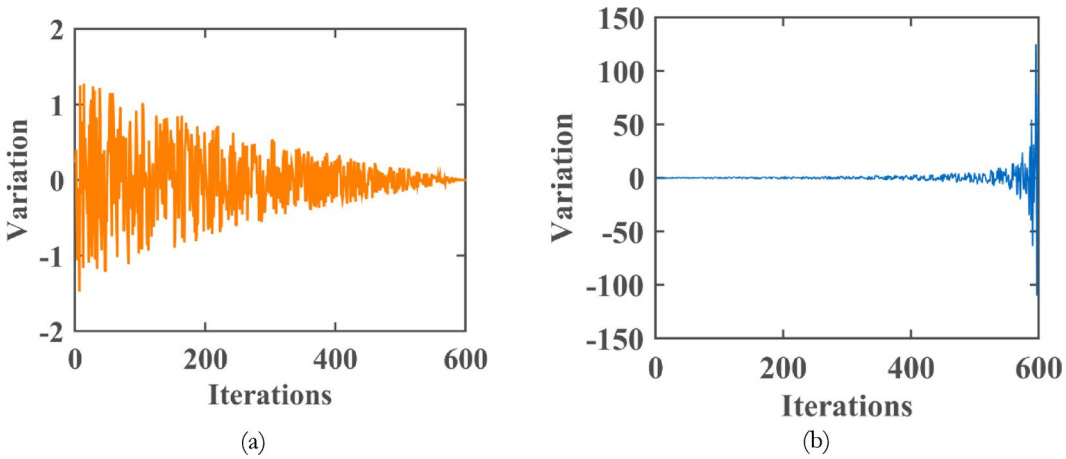

Fig. 15. Refraction parameters in the second half refraction strategy: (**a**)Trends of $Para_1$ (**b**) Trends of $Para_2$[51].

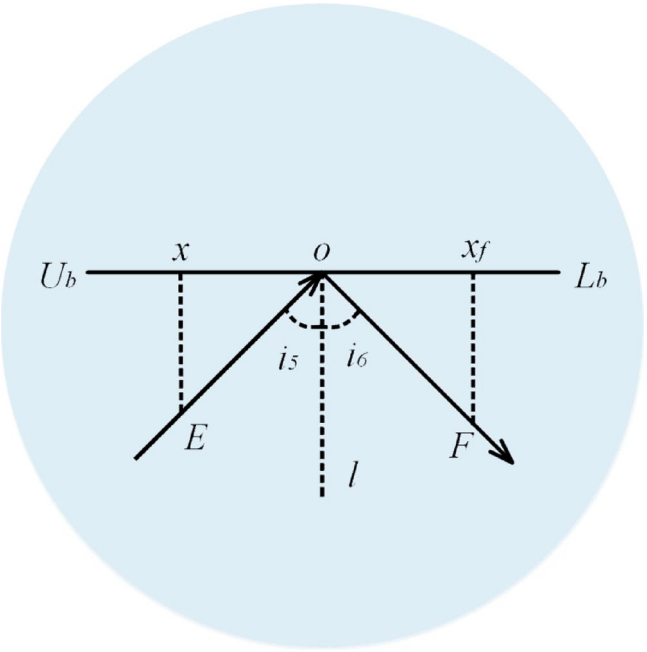

Fig. 16. Total internal reflection process of light[51].

optima by overcoming stagnation in local optima. Equations (14–17) detail the mathematical formulation of this strategy, ensuring precise adjustments based on the geometry of the light propagation and reflection process.

$$x^{next} = x_f = 0.5 \bullet (\alpha + 1)(U_b + L_b) - \alpha x \tag{42}$$

$$\alpha = \frac{F}{E} \tag{43}$$

$$x_0 - x_f = \frac{F \bullet (x - x_0)}{E} \tag{44}$$

$$x_0 = \frac{U_b - L_b}{2} + L_b = \frac{U_b + L_b}{2} \tag{45}$$

The individual x_f is generated through the total internal reflection strategy. The parameter α represents the reflectance of this strategy and governs the transformation pattern of the light individual. When α exceeds 1, the new individual x^{next} crosses the defined boundary, with α constrained to the interval $[0,1]$. The specifics of α 's value will be explored further in Sect. 4.2. Here, U_b and L_b denote the upper and lower boundaries of the individual's position, respectively.

To provide a comprehensive understanding of FATA, Algorithm 2 presents its pseudocode, while Fig. 17 illustrates the workflow, highlighting the two core population updating mechanisms. The algorithm follows a structured process consisting of population initialization, parameter configuration, and an iterative evolution phase. Within this phase, the computational burden of both the mirage light filtering and light refraction strategies is primarily determined by the number of iterations, resulting in a time complexity of $O(n(MaxFEs \bullet d))$.

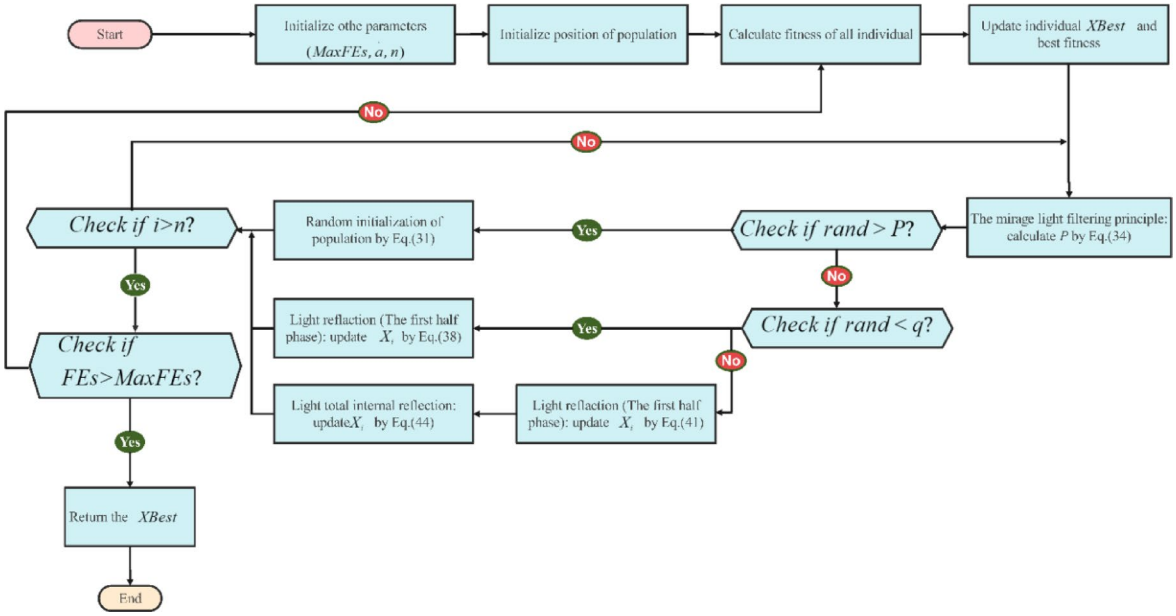

Fig. 17. The flowchart of the FATA[51].

Input: parameters $n, d, MaxFEs$;

Output: optimal Individual;

Initialize parameters $Para_1$, $Para_2$, α;

Generate an initial population x of size n;

Evaluate the fitness of each individual;

While ($FEs \leq MaxFEs$**) do**

Update the best fitness value and store the best individual $best\ fitness, x_{best}$;

Compute weight factors P using Eq. (34);

Determine $Para_1$ and $Para_2$ using Eq. (40) and Eq. (47);

For each individual $i = 1$ to n do

Apply Algorithm 1 to implement the mirage light filtering mechanism;

If $rand > P$, initialize the population randomly using Eq. (31).

Else

If $rand < q$, Update x_i based on the first-phase light refraction strategy using Eq. (38).

Else

Adjust x_i according to the **second-phase light refraction strategy** (Eq. 41).

Further refine x_i using **the total internal reflection mechanism** (Eq. 44).

End If

End If

End For

$t = t + 1$;

Algorithm 2. Pseudocode of FATA

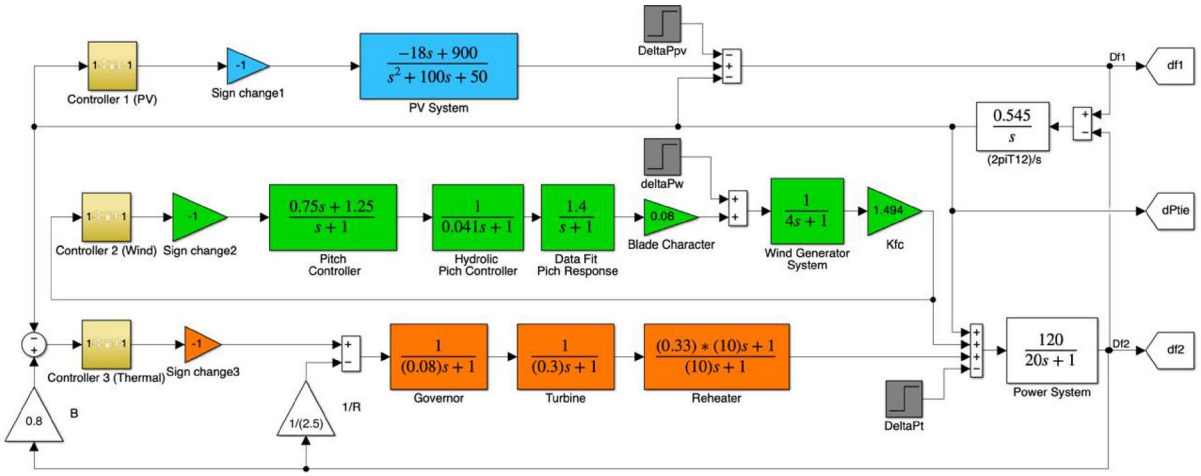

Fig. 18. Simulation system.

Controller	Opt. Alg.	K_{p1}	K_{i1}	K_{p2}	K_{i2}	K_{p3}	K_{i3}	ITAE
PI	**GJO**	0.5251	0.1310	3.9961	−0.0146	2.5244	0.1438	**1.5849**
	ECO	0.49747	0.3525	3.3686	−0.021695	2.6645	0.71119	2.7082
	ESC	0.66383	0.14652	3.9752	−0.0026187	2.4988	0.22543	1.7212
	FATA	0.95732	0.082446	1.7621	−0.0072356	1.1953	1.1022	4.959

Table 7. PI controller parameters with ITAE values.

Controller 1	Optimization Algorithms	K_{p1}	K_{i1}	K_{d1}	n_1
PIDn	GJO	2.9666	0.2723	2.4420	145.8440
	ECO	0.9838682	0.3387465	0.4080806	194.7095
	ESC	3.509963	0.2967109	1.076755	95.23372
	FATA	3.72744	1.787188	1.018562	155.9837

Table 8. PIDn controller 1(PV) parameters.

Controller 2	Optimization Algorithms	K_{p2}	K_{i2}	K_{d2}	n_2
PIDn	GJO	0.1865	5.8383e-04	−0.0010	1.5955
	ECO	−0.1158584	0.1360314	−0.8529435	2.419207
	ESC	0.471755	−0.04236771	3.153995	105.7223
	FATA	2.114036	−0.007076795	0.5647366	144.5859

Table 9. PIDn controller 2 (Wind) parameters.

Simulation and experimental results

In this study, the control of a two-area power system powered by three different energy sources was investigated using PI, PIDn, FOPI, and PPIDn controllers. The parameters of these controllers were optimized using GJO, ECO, ESC, and FATA algorithms.

Subsequently, the obtained results were validated through OPAL-RT, and a comparative analysis was conducted between the simulation outcomes and experimental results. The simulated system is illustrated in Fig. 18.

The mapping of the controllers is defined as Controller 1 – PV system, Controller 2 – Wind system, and Controller 3 – Thermal system. This configuration ensures clear identification and consistency with the corresponding parameter tables (Tables 7, 8, 9, 10, 11, 12, 13, 14, 15 and 16), where the same controller indices are used for comparative and optimization analyses.

Controller 3	Optimization Algorithms	K_{p3}	K_{i3}	K_{d3}	n_3	ITAE
PIDn	GJO	4	4	0.4301	9.0091	0.1958
	ECO	3.999821	3.999953	0.3454577	179.8215	0.2531
	ESC	3.977549	3.928608	0.4525752	11.23297	0.19669
	FATA	4	3.973674	0.524713	7.918286	**0.18676**

Table 10. PIDn controller 3 (Thermal) parameters with ITAE values.

Controller	Optimization Algorithms	K_{p1}	K_{i1}	λ_1	K_{p2}	K_{i2}	λ_2
FOPI	GJO	−0.0027	0.8845	0.4591	3.0071	−0.2188	0.3792
	ECO	−0.39365	1.5131	0.29532	−1.2835	2.8498	0.0001
	ESC	0.77817	0.51205	0.33906	2.3735	−0.2992	0.22255
	FATA	0.33822	0.23075	0.40761	0.89628	0.0073297	0.54136

Table 11. FOPI controller 1 and 2 parameters.

Controller	Optimization Algorithms	K_{p3}	K_{i3}	λ_3	ITAE
FOPI	GJO	2.3013	0.2927	2.7284e-04	2.1444
	ECO	3.8094	−0.83418	0.49918	**2.0176**
	ESC	2.4733	−0.35033	0.52696	2.7095
	FATA	0.38526	0.892	0.49146	7.4598

Table 12. FOPI controller 3 parameters and ITAE values.

Controller 1	Optimization Algorithms	K_{p1}	K_{i1}	K_{d1}	n_1	K_{prd1}	Kh_1
PPIDn	GJO	0.9840	0.2482	3.0399	150.5947	0.0150	0.0299
	ECO	4	1.599685	3.750207	108.2514	3.877172	0
	ESC	3.924731	1.062002	3.218801	115.3733	0.0484639	0.1878636
	FATA	1.170467	0.2721576	1.089585	53.07538	0	0

Table 13. PPIDn controller 1(PV) parameters.

Controller 2	Optimization Algorithms	K_{p2}	K_{i2}	K_{d2}	n_2	K_{prd2}	Kh_2
PPIDn	GJO	−0.0331	−0.0477	5.5685e-05	1.4783	2.0418	1.1120
	ECO	4	0.006105196	−3.256132	99.70377	3.887082	0
	ESC	3.992627	−0.01261917	3.945147	1.001308	0.01774135	0.0471736
	FATA	1.184828	0.2753649	0.9450793	116.2314	4	1.745256

Table 14. PPIDn controller 2 (Wind) parameters.

Controller 3	Optimization algorithms	K_{p3}	K_{i3}	K_{d3}	n_3	K_{prd3}	Kh_3
PPIDn	GJO	4	4	0.7174	10.9674	0	0.0063
	ECO	3.608775	3.309643	0.5120614	152.9706	0.006157692	0.2757894
	ESC	3.979733	3.990961	0.8278113	11.4859	0.07643719	1755.635e-6
	FATA	1.633781	4	1.895669	193.2236	1.867529	0

Table 15. PPIDn controller 3 (Thermal) parameters.

Controller	Optimization algorithms	ITAE
PPIDn	GJO	0.6218
	ECO	0.60473
	ESC	**0.3896**
	FATA	1.6889

Table 16. PPIDn controller ITAE parameters.

Variable	Value	Unit	Unite
a	−18	---	PV Solar Power
b	900	---	PV Solar Power
c	100	---	PV Solar Power
d	50	---	PV Solar Power
D	43	meter	Wind Turbine
a_s	1452	m^2	Wind Turbine
ρ	1.225	kg/m^3	Wind Turbine
H	40	m	Wind Turbine
ω_r	27.2/18.1	rpm	Wind Turbine
P_{wt}	600	kW	Wind Turbine
C_P	0.59	---	Wind Turbine
K_{p1}	1.25	p.u. MW	Wind Energy
K_{p2}	1	p.u. MW	Wind Energy
K_{p3}	1.4	p.u. MW	Wind Energy
K_{pc}	0.08	---	Wind Energy
K_{fc}	1.494	---	Wind Energy
T_{p1}	0.6	s	Wind Energy
T_{p2}	0.041	s	Wind Energy
T_{p3}	1	s	Wind Energy
T_w	4	s	Wind Energy
P_R	200	MW	Thermal System
P_L	100	MW	Thermal System
R_1	2.5	Hz/p.u. MW	Thermal System
B	0.8	p.u. MW/Hz	Thermal System
K_{gov}	1	p.u. MW	Thermal System
T_{gov}	0.08	s	Thermal System
K_{tur}	1	p.u. MW	Thermal System
T_{tur}	0.3	s	Thermal System
K_{reh}	0.33	p.u. MW	Thermal System
K_{ps}	120	Hz/p.u. MΩ	Thermal System
T_{ps}	20	s	Thermal System
T_{reh}	10	s	Thermal System
$2\varphi T_{12}$	0.545	p.u.	Thermal System
a_{12}	−1	---	Thermal System
f	60	Hz	Thermal System

Table 17. System parameter values used in simulation[43].

Parameters

In this study, four different controllers were optimized using four distinct algorithms, resulting in a total of 16 optimization scenarios. The optimization process was conducted with a population size of 50 and 100 iterations for each algorithm.The solar panel model was based on an ambient temperature of 27 °C and a solar irradiance of 1000 W/m^2. The wind energy system consisted of 55 wind turbines. The simulations were performed in the MATLAB/Simulink environment using transfer function-based modeling. Some of the wind turbine parameters listed in Table 17 are provided for informational purposes.

The values of the parameters used in the simulations are summarized in Table 17.

Here, R is the governor speed regulation constant and B shows the frequency bias parameter, H is hub height and K_{pc} is blade character[43].

Variable	Lower	Upper
K_P	−4	4
K_I	−4	4
K_D	−4	4
K_{prd}	0	4
K_h	0	2
n	1	200
λ	0.0001	1

Table 18. The controller parameters limits.

The lower and upper limits of the controllers used in the study are presented in Table 18. The optimization algorithms search for optimal parameters within these predefined ranges.

To establish these limits, a preliminary analysis was conducted. Initially, the best possible values were determined using the Ziegler-Nichols method and trial-and-error approaches. The search range was then set to encompass these values. Additionally, parameter ranges from previous studies in the literature were considered when defining the search space.

The simulation was conducted by applying a 10% load increase to each region in the system.

Simulation

In the simulation studies, PI, PIDn, FOPI, and PPIDn controllers were implemented. The parameters of each controller were optimized using GJO, ECO, ESC, and FATA algorithms within the search space defined in Table 18, aiming to determine the best possible values. A total of 16 different simulations were conducted.

For each optimization algorithm, the population size was set to 50, and the number of iterations was fixed at 100. The performance of the optimization algorithms was evaluated using the ITAE criterion as a reference.

The best parameter values obtained for PI controllers using different optimization algorithms are presented in Table 7. The lowest ITAE value, 1.5849, was achieved using the GJO algorithm.

The optimization results for the PIDn controller are presented collectively in Tables 8, 9 and 10. The data is divided into three sections:

- Table 8 displays the results for the solar energy system controller.
- Table 9 presents the results for the thermal energy system controller.
- Table 10 provides the results for the wind energy system controller.

Among these, the best ITAE value was achieved using the FATA algorithm, with a value of 0.18676.

The optimization results for the FOPI controller are presented in Tables 11 and 12.

- Table 11 provides the optimized parameters for FOPI controllers 1 and 2.
- Table 12 lists the parameters for FOPI controller 3 along with the corresponding ITAE values.

Among the tested algorithms, the lowest ITAE value (2.0176) was obtained using the ECO algorithm.

The optimization results for the PPIDn controller are presented in Tables 13, 14, 15 and 16.

- Table 13 provides the optimized parameters for the solar energy system controller.
- Table 14 presents the parameters for the thermal energy system controller.
- Table 15 lists the parameters for the wind energy system controller.
- Table 16 summarizes the ITAE values obtained using different optimization algorithms for the PPIDn controller.

Among the tested algorithms, the ESC algorithm achieved the lowest ITAE value of 0.3896.

The convergence curves of the PI, PIDn, FOPI, and PPIDn controllers are illustrated in Figs. 19, 20, 21 and 22.

- Figures 20 and 22 provide a more detailed visualization of the curves for better clarity.
- Figs. 19 and 21 do not require detailed plotting, as the general trends are sufficiently visible.

In Fig. 19, the GJO algorithm achieved the lowest ITAE value, which, as shown in Table 7, is 1.5849.

Figure 20 presents the optimization results for the PIDn controller. Among the tested algorithms, the FATA algorithm achieved the lowest ITAE value of 0.18676, indicating superior performance. This trend is clearly observed in the magnified section of the figure and is further validated by the results in Table 10.

Figure 21 illustrates the optimization results for the FOPI controller using ECO, ESC, FATA, and GJO algorithms. The vertical axis represents the best fitness value, while the horizontal axis shows the number of iterations. Among the tested algorithms, ECO achieved the lowest ITAE value of 2.0176, indicating the best optimization performance for this controller. As seen in the figure, GJO (black) and ECO (blue) exhibit rapid initial convergence, whereas FATA (green) stagnates at a higher fitness level, suggesting ineffective parameter tuning. The ESC (red) algorithm shows a moderate convergence rate, stabilizing at a slightly higher ITAE value than ECO. The results indicate that ECO effectively balances exploration and exploitation, leading to faster

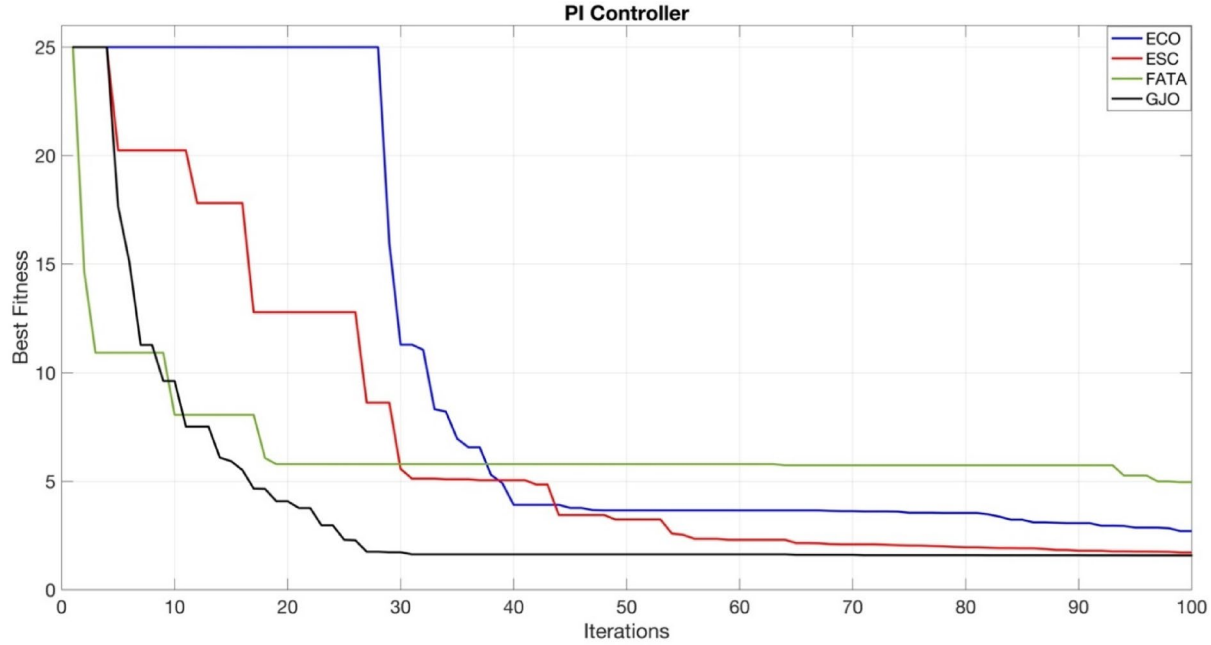

Fig. 19. Convergence curve for PI controller.

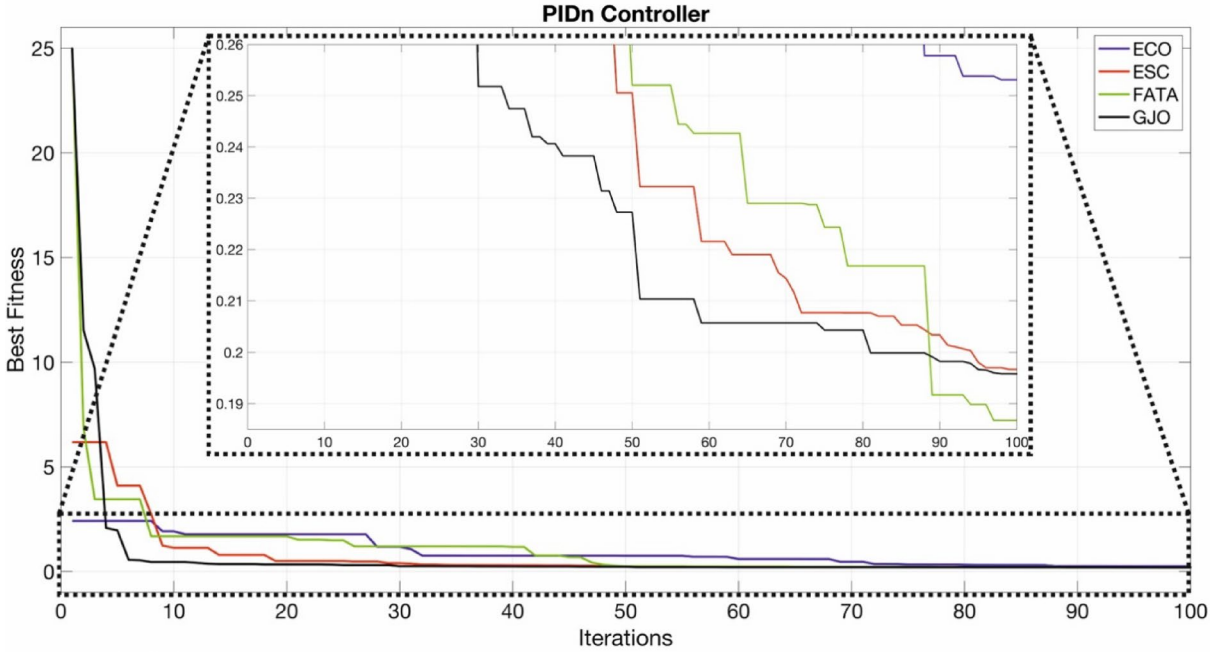

Fig. 20. Convergence curve for PIDn controller.

convergence and lower ITAE values. In contrast, FATA struggles to refine the solution after early iterations, possibly due to its search strategy. This finding aligns with previous studies where ECO has demonstrated robust performance in fine-tuning controller parameters.

Figure 22 illustrates the optimization results for the PPIDn controller using ECO, ESC, FATA, and GJO algorithms. The best fitness values are plotted against the number of iterations, with a zoomed-in section highlighting the finer details of the convergence behavior. Among the tested algorithms, ESC achieved the lowest ITAE value of 0.3896, indicating superior optimization performance. As seen in the figure, ESC (red) exhibits rapid convergence and stabilizes at a lower fitness value compared to the other algorithms. ECO (blue) and GJO (black) also show stable convergence, but at slightly higher ITAE values. FATA (green), on the other hand, stagnates at a higher fitness level, suggesting suboptimal tuning. The results suggest that ESC effectively balances

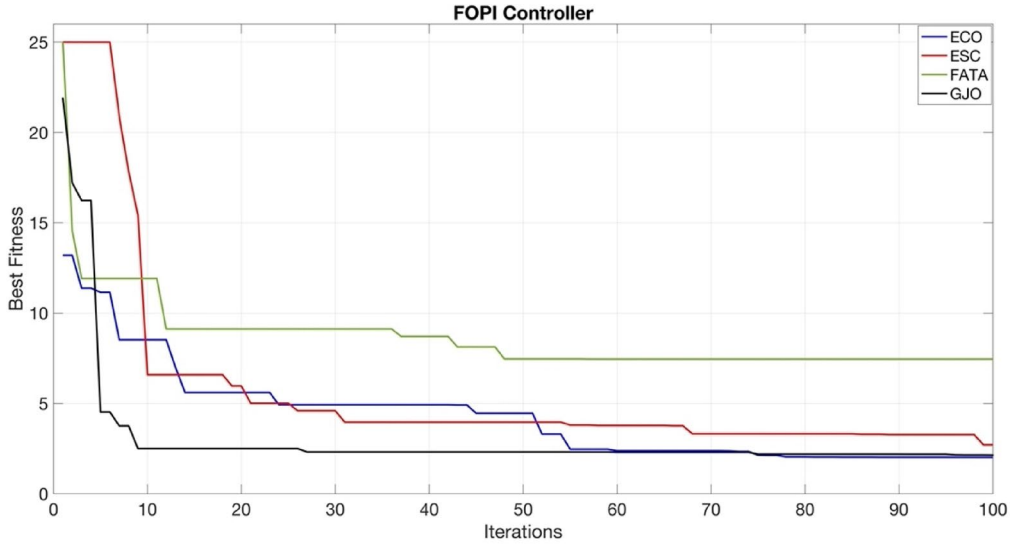

Fig. 21. Convergence curve for FOPI controller.

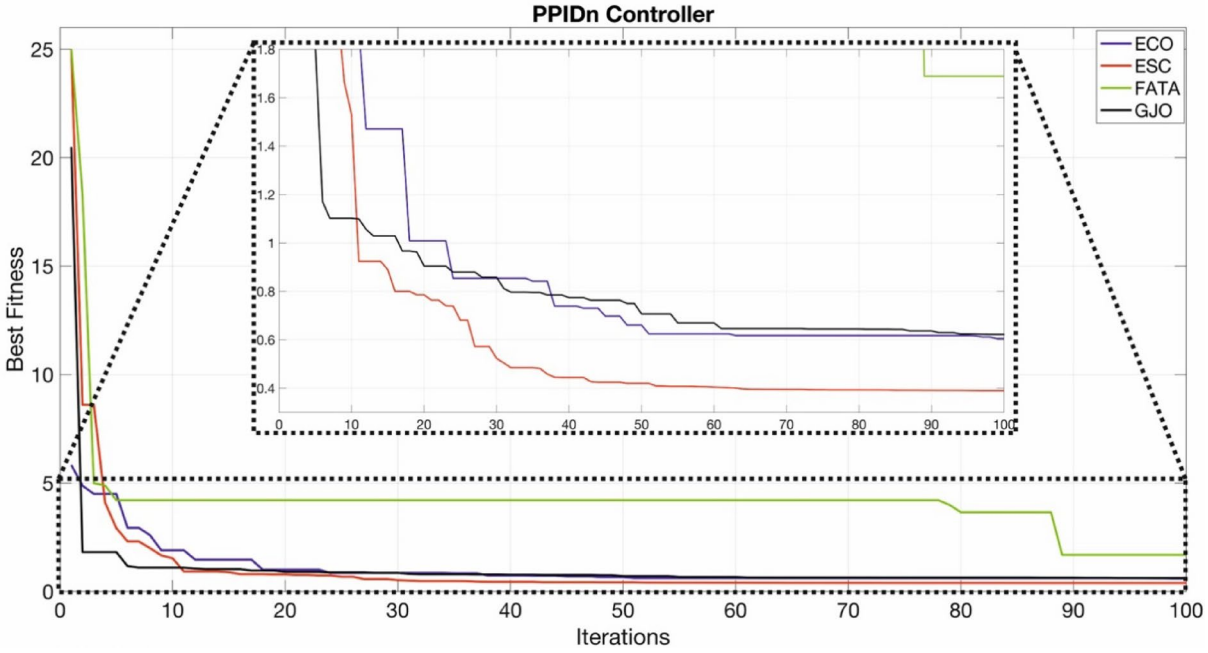

Fig. 22. Convergence curve for PPIDn controller.

exploration and exploitation, allowing it to converge to an optimal solution more efficiently. The detailed section in Fig. 22 further highlights this advantage by showcasing the faster fitness improvement of ESC compared to the other methods. These findings reinforce the effectiveness of ESC in optimizing PPIDn controller parameters for this system.

Table 19 presents the optimized PIDn controller parameters obtained using the FATA algorithm, as demonstrated in Tables 8 and 9, and 10. These parameters were derived from 16 different simulation studies, where the FATA algorithm achieved the lowest ITAE value of 0.18676.

As seen in Table 19, the optimal values for K_p, K_i, K_d, and n were determined for each region. These values were fine-tuned to enhance system performance, ensuring improved frequency stability and dynamic response. The low ITAE value indicates the effectiveness of FATA in optimizing PIDn controllers, making it a strong candidate for load frequency control in multi-area power systems.

Figure 23 presents the system responses obtained using the best-optimized parameters for each controller (PI, PIDn, FOPI, and PPIDn). The figure illustrates the frequency deviations in each region (Δf_1 and Δf_2) as well as the tie-line power deviation (ΔP_{tie}) over the time. As shown, the PPIDn-ESC controller (red) provides

Cont.	Alg.	T_S (Settling Time)			U_S (Undershoot)			O_S (Overshoot)		
		Δf_1	Δf_2	Δf_{tie}	Δf_1	Δf_2	Δf_{tie}	Δf_1	Δf_2	Δf_{tie}
PI	GJO	12	13	12	−0.13	−0.18	−0.0285	0.0139	0.0345	0.014
PIDn	FATA	**4**	**4**	**4**	**−0.09**	**−0.09**	**−0.0023**	0.05	0.0384	0.00153
FOPI	ECO	11	12	---	−0.11	−0.165	−0.0215	**0.011**	0.0283	0.01
PPIDn	ESC	6	6	**4**	−0.12	−0.12	−0.0025	0.02	**0.018**	**0.00077**

Table 19. Comparison of the best results obtained with optimization algorithms for all controllers in terms of T_S, U_S, and O_S.

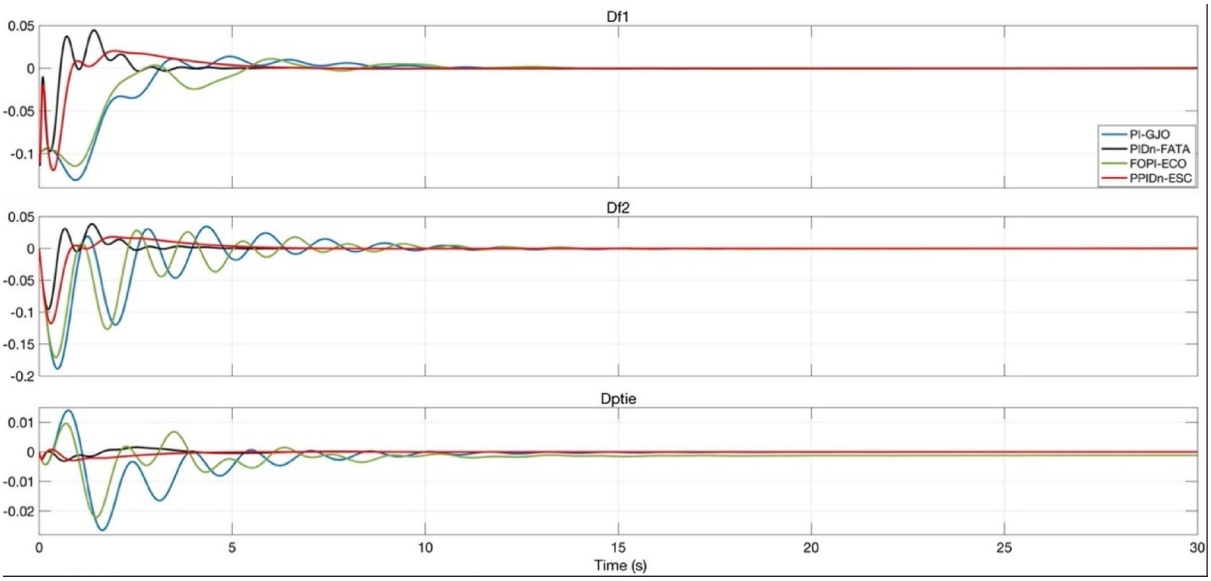

Fig. 23. System responses with the best-tuned parameters for PI, PIDn, FOPI, and PPIDn controllers.

the fastest settling time and minimal oscillations, indicating superior performance in stabilizing frequency fluctuations. The PIDn-FATA (green) and FOPI-ECO (blue) controllers exhibit relatively higher oscillations but still converge to a stable state. In contrast, the PI-GJO controller (black) shows the largest initial deviations and prolonged oscillations, suggesting slower stabilization. These results confirm that ESC-optimized PPIDn achieves the best dynamic response, effectively minimizing frequency deviations and ensuring system stability in a multi-area power system.

Figure 24 provides a more detailed view of the system responses, illustrating the frequency deviations Δf_1 and Δf_2 in each region and the tie-line power deviation ΔP_{tie} over a shorter time interval.

Compared to Fig. 23, this zoomed-in representation allows for a clearer analysis of the initial transient behavior and oscillatory characteristics of each controller. The differences in settling time, peak overshoot, and damping performance among the PI-GJO, PIDn-FATA, FOPI-ECO, and PPIDn-ESC controllers can be observed more precisely.

Table 19 presents a comparative analysis of the settling time (T_S), undershoot (U_S), and overshoot (O_S) values for the frequency deviations shown in Fig. 24, based on the optimized parameters of each controller.

Among the tested controllers, the PIDn controller optimized with FATA achieved the best results in terms of settling time and undershoot, demonstrating faster stabilization and minimal deviations. On the other hand, the PPIDn controller optimized with ESC exhibited the lowest overshoot values, indicating superior damping performance. The FOPI controller optimized with ECO provided the best overshoot performance only for the first region's frequency deviation. Meanwhile, the PI controller failed to achieve competitive results across any of the evaluated criteria, performing worse than the other controllers.

Experimental results

The OPAL-RT OP5707 platform was utilized to validate the real-time performance of the proposed controllers. This hardware-based environment allows the assessment of control algorithms under realistic conditions, including finite sampling intervals, communication delays, and numerical precision effects that are not fully captured in offline simulations. Such validation ensures that the proposed FATA-optimized controller is not only theoretically efficient but also practically reliable for real-world power system applications.

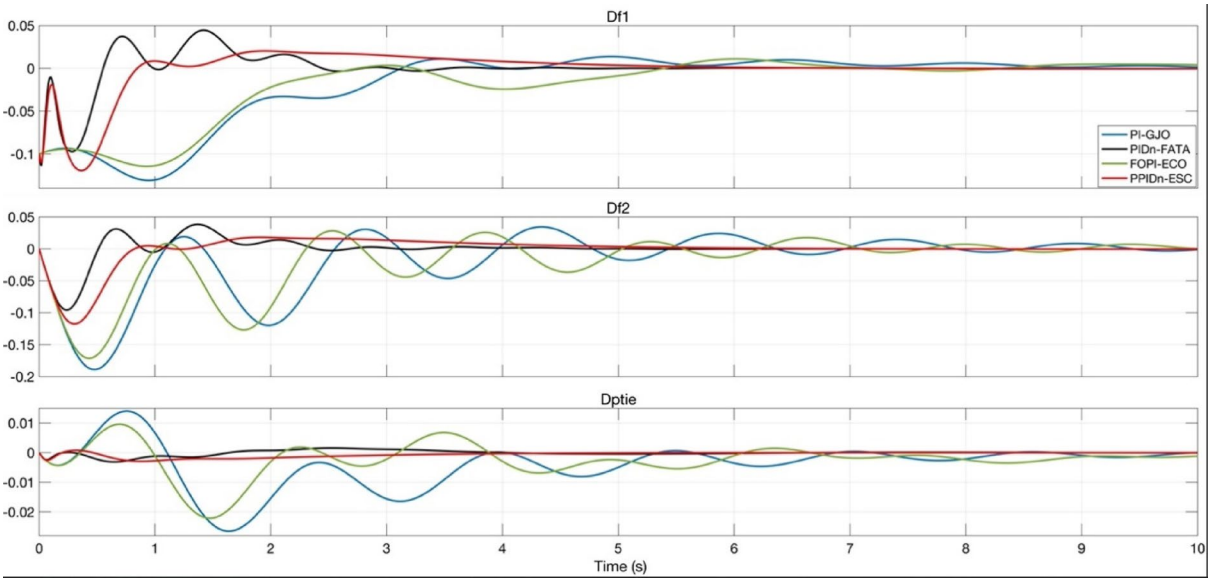

Fig. 24. Detailed system responses with the best-tuned parameters for PI, PIDn, FOPI, and PPIDn controllers.

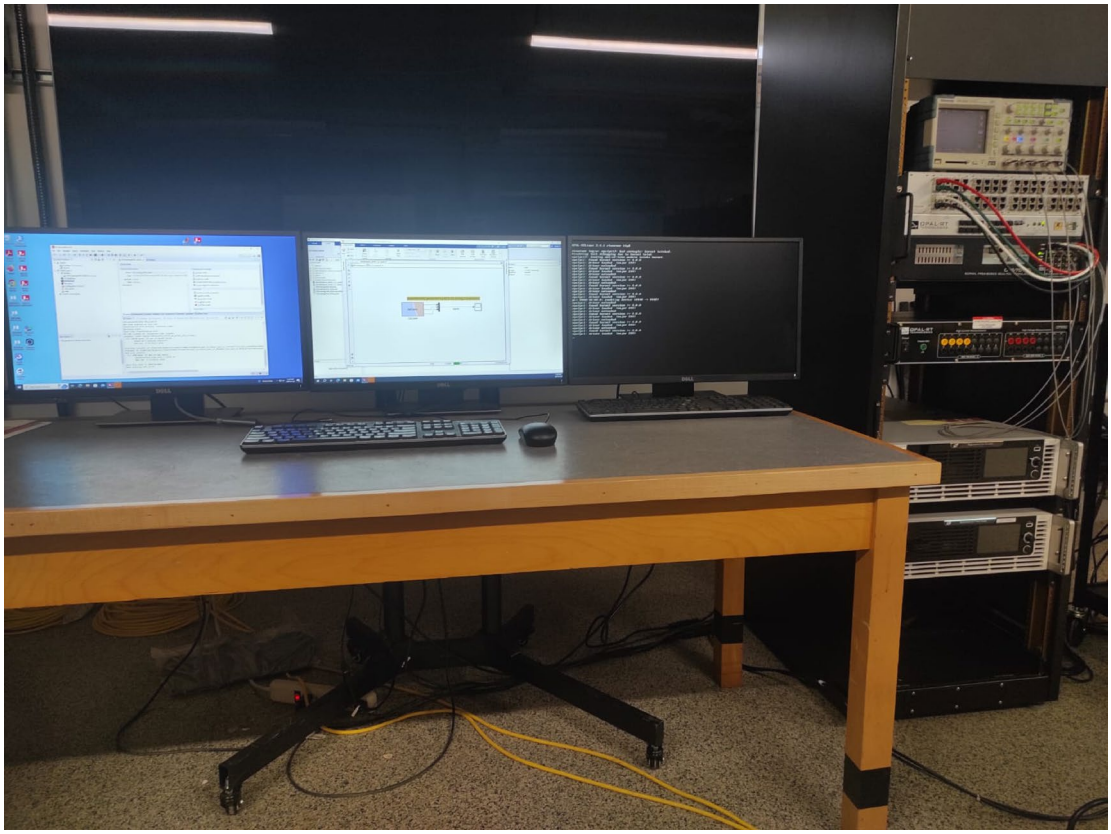

Fig. 25. OPAL-RT experimental setup.

Among all the evaluated controllers, the PIDn controller achieved the best performance. Its parameters were optimized using the FATA algorithm, as presented in Table 7. To verify the reliability of these results, the optimized parameters were implemented on the OPAL-RT platform, and the experimental outcomes were compared with the simulation results. The experimental setup used for real-time validation is shown in Fig. 25.

The objective of this section is to validate the simulation outcomes Matlab/Simulink program in the context of real-time implementation of the proposed approach. For this purpose, this process is illustrated as shown

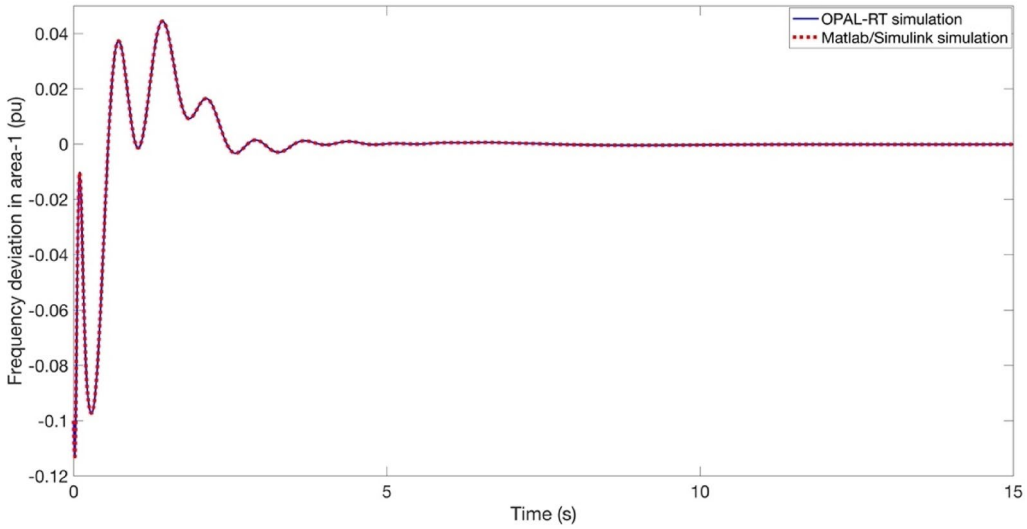

Fig. 26. OPAL-RT result of Δf_1.

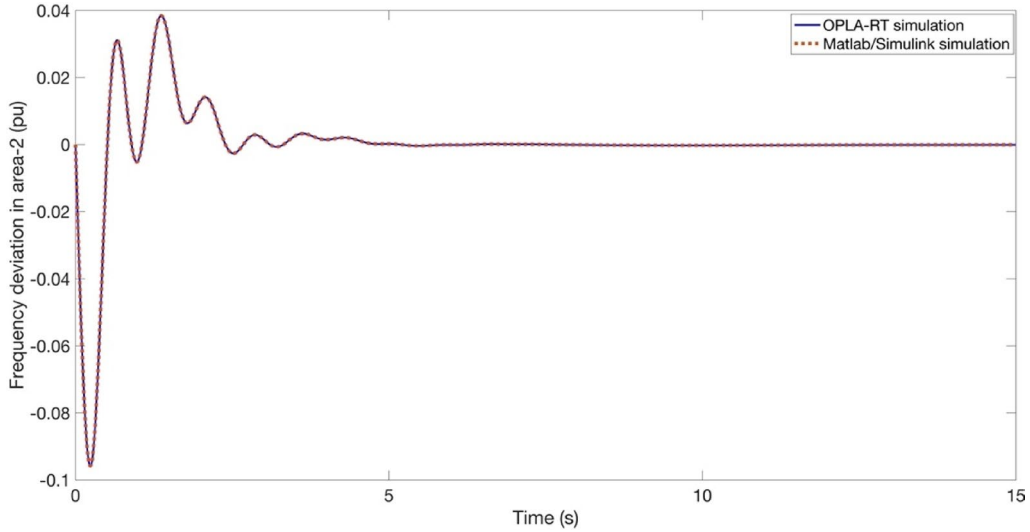

Fig. 27. OPAL-RT result of Δf_2.

in Fig. 25. It is imperative to acknowledge that the outcomes of the OPAL-RT investigations are influenced by intrinsic delay and error components that are not present in conventional offline implementations. As shown in Figs. 26 and 27, and 28, the time domain responses of the Δf_1, Δf_2, and ΔP_{tie} based on the FATA-PIDn controller are depicted, with these responses being based on the real-time simulator OPAL-RT. As evidenced by Fig. 25, the results obtained from the MATLAB simulation software demonstrate a notable degree of similarity to those produced by the OPAL-RT real-time simulator.

Figures 26 and 27, and 28 present the experimental and simulation results obtained using the PIDn controller optimized with the FATA algorithm. These figures compare the real-time performance of the controller, demonstrating its effectiveness in practical implementation.

In Fig. 26, the Δf_1 in area-1 is depicted. The results from the OPAL-RT experimental setup and Matlab/Simulink simulation are shown together, indicating a strong correlation between the experimental and simulation data. This consistency validates the accuracy and reliability of the proposed control approach.

Figure 27 illustrates the Δf_2 in Area 2. The experimental results obtained from the OPAL-RT platform and the Matlab/Simulink simulation show an almost identical response, as the curves overlap perfectly. This strong agreement confirms the accuracy and reliability of the proposed PIDn controller optimized with the FATA algorithm in real-time implementation.

Figure 28 illustrates the power deviation at the tie-line between the two areas. The experimental results from the OPAL-RT platform and the Matlab/Simulink simulation are perfectly aligned, demonstrating an exact

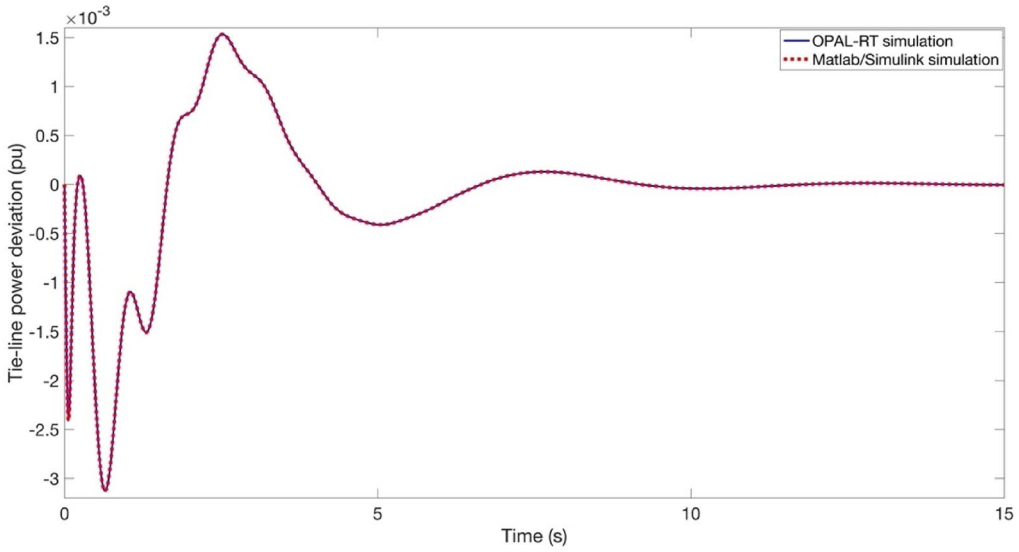

Fig. 28. OPAL-RT result of ΔP_{tie}.

match. This strong correlation confirms the accuracy and reliability of the proposed PIDn controller optimized with the FATA algorithm in maintaining frequency stability across interconnected regions.

It is again noteworthy that the OPAL-RT hardware inherently involves minor latency and dead-time effects caused by real-time signal processing and data communication. Despite these practical nonlinearities, the experimental results obtained from the OPAL-RT platform closely matched the MATLAB/Simulink simulations. Therefore, the proposed model and controller design are considered sufficiently accurate and robust for realistic operating conditions.

Discussion

In this study, PI, PIDn, FOPI, and PPIDn controllers were implemented to regulate frequency in a two-area power system with three different energy sources. The parameters of these controllers were optimized using GJO, ECO, ESC, and FATA algorithms. Among the 16 different optimization scenarios, the PIDn controller optimized with the FATA algorithm demonstrated the best performance in simulation studies.

To validate these results, the optimized parameters were tested on the OPAL-RT real-time simulation platform. The experimental results closely matched the simulation outcomes, with overlapping response curves confirming the accuracy and reliability of the proposed control strategy.

Based on the findings, the following key conclusions can be drawn:

- Despite its more complex structure, the PPIDn controller did not outperform the PIDn controller, which achieved the best results among the tested controllers.
- The selected optimization algorithms were chosen based on their potential to effectively address frequency deviation issues in a two-area power system.
- Simulation runtime influences optimization performance, and a population size of 50 with 100 iterations was considered sufficient for the optimization process.
- Since ITAE values change over time, longer simulation durations result in higher ITAE values. Therefore, the simulation time must be carefully selected to ensure a meaningful comparison.
- The experimental validation of the results confirms the accuracy and correctness of the optimization process, demonstrating the practical applicability of the proposed method.

When the obtained results are compared with similar studies in the literature, it is observed that in the study where PI/PID/PDn-PI cascade controllers were tested, the controller parameters were optimized using the Coyote optimization algorithm. During a 30-second simulation period, the ITAE value was measured, and the best result of 1.935 was achieved with the PDn-PI controller. In the present study, however, a significantly improved ITAE value of 0.18676 was obtained[48].

In conclusion, for the considered power system, the PIDn controller optimized with FATA exhibited the best overall performance, effectively improving frequency stability and system response.

Conclusion and recommendations

Based on this study, the following recommendations are provided for researchers conducting similar work:

- The most effective controller cannot always be predicted in advance. In some cases, even the simplest controllers may yield the best results.

- Exploring different optimization algorithms may lead to improved outcomes. Testing alternative methods could further enhance performance.
- Increasing the population size and the number of iterations can improve optimization results. However, this also increases computational time. Therefore, unnecessary simulation time should be avoided, particularly by considering the settling time as a critical factor.
- Utilizing more advanced computing systems can significantly reduce processing time, enabling more efficient optimization.
- Additionally, the findings from the simulation study validate the effectiveness of the FATA-PIDn controller developed for a two-area, three-source LFC system. This conclusion is supported by real-time OPAL-RT-based simulations, confirming the practical applicability of the proposed method in a realistic operational environment.
- Although the present study focused on validating the performance of the FATA-based controllers, future research will include a detailed computational complexity assessment, sensitivity and stability analyses to provide a more comprehensive understanding of system behavior.

Data availability

All relevant data are within the manuscript. The collection and analysis method complied with the terms and conditions for the source of the data.

Received: 11 August 2025; Accepted: 3 November 2025
Published online: 08 December 2025

References

1. Saadat, H. *Power System Analysis* p. 527–576 (McGraw-Hill, 1999).
2. Ranjan, M. & Shankar, R. A literature survey on load frequency control considering renewable energy integration in power system: recent trends and future prospects. *J. Energy Storage*. **45**, 103717. https://doi.org/10.1016/j.est.2021.103717 (2022).
3. Ali, H., Magdy, G. & Xu, D. A new optimal robust controller for frequency stability of interconnected hybrid microgrids considering non-inertia sources and uncertainties. *Int. J. Electr. Power Energy Syst.* **128**, 106651. https://doi.org/10.1016/j.ijepes.2020.106651 (2021).
4. Pati, S. S. & Subudhi, U. Stability analysis of a Multi-area renewable system and frequency control with improved chaotic Harris Hawk optimization algorithm. *Arab. J. Sci. Eng.* **49**, 6531–6550. https://doi.org/10.1007/s13369-023-08313-7 (2024).
5. Arya, Y. A novel CFFOPI-FOPID controller for AGC performance enhancement of single and multi-area electric power systems. *ISA Trans.* **100**, 126–135. https://doi.org/10.1016/j.isatra.2019.11.025 (2020).
6. El-Khatib, M. F., Khater, F. M. H., Hendawi, E. & Abu El-Sebah, M. I. Simplified and intelligent controllers for multi-input multi-output processes. *Eng. Appl. Artif. Intell.* **141**, 109816. https://doi.org/10.1016/j.engappai.2024.109816 (2025).
7. Patel, N. C. & Sahu, B. K. Design and implementation of FIPID controller for LFC of Multi-unit Multi-source Linear/Non-linear power system. *Technol. Econ. Smart Grids Sustain. Energy*. **6**, 1–17. https://doi.org/10.1007/s40866-021-00121-y (2021).
8. Kumari, N., Aryan, P., Raja, G. L. & Arya, Y. Dual degree branched type-2 fuzzy controller optimized with a hybrid algorithm for frequency regulation in a triple-area power system integrated with renewable sources. *Prot. Control Mod. Power Syst.* https://doi.org/10.1186/s41601-023-00317-7 (2023).
9. Soliman, A. M. A., Bahaa Eldin, M. & Ahmed Mehanna, M. Application of WOA tuned Type-2 FLC for LFC of two area power system with RFB and solar park considering TCPS in interline. *IEEE Access.* **10**, 112007–112018. https://doi.org/10.1109/ACCESS.2022.3215530 (2022).
10. Shukla, S. & Jha, S. K. Improved Grey Wolf Optimization Abetting Fuzzy Logic Controllers Used for Load Frequency Control in Two-Area Interlinked Reheat Thermal Power Plants applying Governor Dead Band and Generation Rate Constraint Non-Linearity. *Proc. 2nd Int. Conf. Intell. Innov. Technol. Comput. Electr. Electron. ICIITCEE* https://doi.org/10.1109/IITCEE59897.2024.10467330 (2024).
11. Shankar, R., Chatterjee, K. & Chatterjee, T. K. Genetic algorithm based controller for load-frequency control of interconnected systems. *1st Int. Conf. Recent. Adv. Inf. Technol. RAIT-2012.* **2012**, 392–397. https://doi.org/10.1109/RAIT.2012.6194452 (2012).
12. Pradhan, C. & Gjengedal, T. Adaptive Jaya Algorithm for Optimized PI-PD Cascade Controller of Load Frequency Control in Interconnected Two-Area Power System. *Proc. 2020 Int. Conf. Smart Syst. Technol. SST 2020* **2020**, 181–186. https://doi.org/10.1109/SST49455.2020.9263701 (2020).
13. Sai Kalyan, C. N. et al. Exhibiting the effect of AVR coupling on the performance of LFC in multi area hybrid power system. *Int. Conf. Emerg. Technol. INCET 2022.* **2022**, 1–6. https://doi.org/10.1109/INCET54531.2022.9824930 (2022). 3.
14. Jameel, A. & Gulzar, M. M. Load frequency regulation of interconnected muli-source multi-area power system with penetration of electric vehicles aggregator model. *Electr. Eng.* **105**, 3951–3968. https://doi.org/10.1007/s00202-023-01923-2 (2023).
15. Rafikiran, S., Prashanth, V., Suneetha, P. & Basha, C. H. Application of battery storage controlling by utilizing the adaptive neural network controller at various local load conditions. InInternational Conference on Computer Vision and Robotics. Feb 24 (pp. 477–486). Singapore: Springer Nature Singapore. (2023).
16. Reddy, K. R. et al. A novel on energy management strategy with maximum exploitation of renewables and EV storage in distribution networks. *Int. Trans. Electr. Energy Syst.* **2023** (1), 1365608 (2023).
17. Ramesh, M., Yadav, A. K., Pathak, P. K. & Hussaian Basha, C. H. A novel fuzzy assisted sliding mode control approach for frequency regulation of wind-supported autonomous microgrid. *Sci. Rep.* **14** (1), 31526 (2024).
18. Reddy, S. V. et al. An Enhanced Repetitive Control Framework for Adaptive Neuro-Fuzzy Learning Grid-Connected Inverter with Current Control and Frequency Adaptability. In2024 Third International Conference on Trends in Electrical, Electronics, and Computer Engineering (TEECCON) Nov 7 (pp. 240–244) (2024).
19. Dorf, R. & Bishop, R. Modern Control Systems. 13th ed. Pearson International; https://elibrary.pearson.de/book/99.150005/9781292152981(2017).
20. Tasnim, M. N., Ahmed, T., Ahmad, S. & Mekhilef, S. Hardware in the loop implementation of the control strategies for the AC-Microgrid in OPAL-RT Simulator. 2023 IEEE IAS glob Conf renew energy Hydrog technol globConHT **2023**:1–6. https://doi.org/10.1109/GlobConHT56829.2023.10087462(2023).
21. Khamari, D., Sahu, R. K., Panda, S. & Arya, Y. A mMSA-FOFPID controller for AGC of multi-area power system with multi-type generations. *Sustain. Comput. Inf. Syst.* **44**, 101046. https://doi.org/10.1016/j.suscom.2024.101046 (2024).
22. Kumar, R. & Prasad, L. B. Optimal load frequency control of multi-area multi-source deregulated power system with electric vehicles using teaching learning-based optimization: a comparative efficacy analysis. *Electr. Eng.* **106**, 1865–1893. https://doi.org/10.1007/s00202-023-02027-7 (2024).

23. Meseret, G. M. & Saikia, L. C. Hybrid neuro-fuzzy-based 3DOF-PDN controller for AGC of multi-area interconnected power system incorporated hydrogen aqua electrolyze fuel cell units and unified power flow controller. *Electr. Eng.* https://doi.org/10.1007/s00202-024-02405-9 (2024).
24. Güler, Y. & Kaya, I. Load frequency control of Single-Area power system with PI–PD controller design for performance improvement. *J. Electr. Eng. Technol.* **18**, 2633–2648. https://doi.org/10.1007/s42835-022-01371-1 (2023).
25. Sahin, E. Design of an optimized fractional high order differential feedback controller for load frequency control of a Multi-Area Multi-Source power system with nonlinearity. *IEEE Access.* **8**, 12327–12342. https://doi.org/10.1109/ACCESS.2020.2966261 (2020).
26. Ojha, S. K. & Maddela, C. O. Load frequency control of a two-area power system with renewable energy sources using brown bear optimization technique. *Electr. Eng.* **106**, 3589–3613. https://doi.org/10.1007/s00202-023-02143-4 (2024).
27. Kalyan, C. N. S. Impact of mechanical and electrical hydro governing systems on the LFC of hydro thermal power system under TIDDF controller. *Microsyst. Technol.* https://doi.org/10.1007/s00542-024-05685-0 (2024).
28. El-Bahay, M. H., Lotfy, M. E. & El-Hameed, M. A. Effective participation of wind turbines in frequency control of a two-area power system using coot optimization. *Prot. Control Mod. Power Syst.* https://doi.org/10.1186/s41601-023-00289-8 (2023).
29. Kumar, R. & Sharma, V. K. Interconnected power control on unequal, deregulated multi-area power system using three-degree-of-freedom-based FOPID-PR controller. *Electr. Eng.* **106**, 2107–2129. https://doi.org/10.1007/s00202-023-02043-7 (2024).
30. Soni, V., Parmar, G. & Kumar, M. A hybrid grey Wolf optimisation and pattern search algorithm for automatic generation control of multi-area interconnected power systems. *Int. J. Adv. Intell. Paradig.* **18**, 265–293. https://doi.org/10.1504/IJAIP.2021.113323 (2021).
31. Xi, L., Wu, J., Xu, Y. & Sun, H. Automatic generation control based on multiple neural networks with Actor-Critic strategy. *IEEE Trans. Neural Networks Learn. Syst.* **32**, 2483–2493. https://doi.org/10.1109/TNNLS.2020.3006080 (2021).
32. Baral, K. K., Sahu, P. C., Barisal, A. K. & Mohanty, B. Combined analysis on AGC and ELD of a hybrid power system with D-WCA designed Gaussian type-2 fuzzy controller. *Evol. Syst.* **14**, 263–280. https://doi.org/10.1007/s12530-022-09454-0 (2023).
33. Priyadarshani, S. & Subhashini, K. R. Search and rescue optimization algorithm tuned FOTID controller for load frequency control of power system. *Iran. J. Sci. Technol. - Trans. Electr. Eng.* **48**, 1045–1067. https://doi.org/10.1007/s40998-024-00724-y (2024).
34. Saikia, N. & Das, N. K. Load frequency control of a two area Multi-source power system with electric vehicle. *J. Control Autom. Electr. Syst.* **34**, 394–406. https://doi.org/10.1007/s40313-022-00974-3 (2023).
35. Chakraborty, S., Mondal, A. & Biswas, S. Application of FUZZY-3DOF-PID controller for controlling FOPTD type communication delay based renewable three-area deregulated hybrid power system. *Evol. Intell.* **17**, 2821–2841. https://doi.org/10.1007/s12065-024-00914-x (2024).
36. Jagatheesan, K., Boopathi, D., Samanta, S., Anand, B. & Dey, N. Grey Wolf optimization algorithm-based PID controller for frequency stabilization of interconnected power generating system. *Soft Comput.* **28**, 5057–5070. https://doi.org/10.1007/s00500-023-09213-6 (2024).
37. Gupta, N. K., Singh, A. & kumar, Mahanty, R. N. Load frequency control with moth-flame optimizer algorithm tuned 2-DOF-PID controller of the interconnected unequal three area power system with and without non-linearity. *Int. J. Syst. Assur. Eng. Manag.* **14**, 1912–1932. https://doi.org/10.1007/s13198-023-02021-z (2023).
38. Nayak, P. C., Prusty, R. C. & Panda, S. Grasshopper optimization algorithm optimized multistage controller for automatic generation control of a power system with FACTS devices. *Prot. Control Mod. Power Syst.* https://doi.org/10.1186/s41601-021-00187-x (2021).
39. Nayak, P. C., Prusty, U. C., Prusty, R. C. & Panda, S. Imperialist competitive algorithm optimized cascade controller for load frequency control of multi-microgrid system. *Energy Sources Part. Recover Util. Environ. Eff.* **47**, 5538–5560. https://doi.org/10.1080/15567036.2021.1897710 (2025).
40. Prusty, U. C., Nayak, P. C., Prusty, R. C. & Panda, S. An improved moth swarm algorithm based fractional order type-2 fuzzy PID controller for frequency regulation of microgrid system. *Energy Sources Part. Recover Util. Environ. Eff.* https://doi.org/10.1080/15567036.2022.2038735 (2025).
41. Nayak, P. C., Nayak, B. P., Prusty, R. C. & Panda, S. Sunflower optimization based fractional order fuzzy PID controller for frequency regulation of solar-wind integrated power system with hydrogen aqua equalizer-fuel cell unit. *Energy Sources Part. Recover Util. Environ. Eff.* **47**, 9550–9568. https://doi.org/10.1080/15567036.2021.1953636 (2025).
42. Mishra, D., Nayak, P. C., Prusty, R. C. & Panda, S. An improved equilibrium optimization-based fuzzy Tilted double integral derivative with filter (F-TIDF-2) controller for frequency regulation of an off-grid microgrid. *Electr. Eng.* **106**, 2033–2055. https://doi.org/10.1007/s00202-023-02054-4 (2024).
43. Sun, J. et al. Towards fast bayesian inference of equivalent circuit parameters of perovskite solar cell. *Sol Energy*. **288**, 113308. https://doi.org/10.1016/j.solener.2025.113308 (2025).
44. Issa, M., Helmi, A. M. & Ghetas, M. Estimation of solar cell parameters through utilization of adaptive sine–cosine particle swarm optimization algorithm. *Neural Comput. Appl.* **36**, 8757–8773. https://doi.org/10.1007/s00521-024-09534-z (2024).
45. Abd-Elazim, S. M. & Ali, E. S. Load frequency controller design of a two-area system composing of PV grid and thermal generator via firefly algorithm. *Neural Comput. Appl.* **30**, 607–616. https://doi.org/10.1007/s00521-016-2668-y (2018).
46. Jeddi, S. A., Hamidreza Abbasi, S. & Shabaninia, F. Load frequency control of two area interconnected power system (diesel generator and solar PV) with PI and FGSPI controller. AISP 2012–16th CSI Int Symp Artif. *Intell. Signal. Process.* https://doi.org/10.1109/AISP.2012.6313803 (2012).
47. Ahmed, S. D., Al-Ismail, F. S. M., Shafiullah, M., Al-Sulaiman, F. A. & El-Amin, I. M. Grid integration challenges of wind energy: A review. *IEEE Access.* **8**, 10857–10878. https://doi.org/10.1109/ACCESS.2020.2964896 (2020).
48. Abou El-Ela, A. A., El-Sehiemy, R. A., Shaheen, A. M. & Diab, A. E. G. Design of cascaded controller based on Coyote optimizer for load frequency control in multi-area power systems with renewable sources. *Control Eng. Pract.* **121**, 105058. https://doi.org/10.1016/j.conengprac.2021.105058 (2022).
49. Amir, M., Zaery, M., Singh, K., Suhail Hussain, S. M. & Abido, M. A. Enhancement of frequency regulation by TFOID controller in hybrid renewable energy with battery storage System-Based Multi-Area microgrids. *IEEE Access.* **12**, 110813–110828. https://doi.org/10.1109/ACCESS.2024.3439738 (2024).
50. Hagglund, T. A predictive PI controller for processes with long dead times. *IEEE Control Syst. Mag.* **12**(1), 57–60. https://doi.org/10.1109/37.120455 (1992).
51. Qi, A. et al. FATA: an efficient optimization method based on geophysics. *Neurocomputing* **607**, 128289. https://doi.org/10.1016/j.neucom.2024.128289 (2024).

Acknowledgements

Erdinç Şahin would like to express gratitude for the support provided by the Scientific and Technological Research Council of Türkiye (TUBITAK) BIDEB 2219 (International Postdoctoral Research Fellowship Program) under application number 1059B192301365. Additionally, we thank the University of New Brunswick, Canada, for their support in utilizing the OPAL-RT device.

Author contributions

Aykut Fatih Güven, Erdinç Şahin: Conceptualization, Methodology, Software, Visualization, Investigation, Writing- Original draft preparation. Onur Özdal Mengi: Data curation, Validation, Supervision, Resources, Writing - Review & Editing. Mohit Bajaj, Viktoriia Bereznychenko: Project administration, Supervision, Resources, Writing - Review & Editing.

Funding

This research received no specific grant from any funding agency in the public, commercial, or not-for-profit sectors.

Declarations

Competing interests

The authors declare no competing interests.

Additional information

Correspondence and requests for materials should be addressed to A.F.G., M.B. or V.B.

Reprints and permissions information is available at www.nature.com/reprints.

Publisher's note Springer Nature remains neutral with regard to jurisdictional claims in published maps and institutional affiliations.